PHYSICAL REVIEW A, VOLUME 64, 033425

Calculations of collisions between cold alkaline-earth-metal atoms in a weak laser field

Mette Machholm
Department of Computational Science, The National University of Singapore, Singapore 119260

Paul S. Julienne
National Institute for Standards and Technology, 100 Bureau Drive, Stop 8423, Gaithersburg, Maryland 20899-8423

Kalle-Antti Suominen
Department of Applied Physics, University of Turku, FIN-20014 Turun yliopisto, Finland;
Helsinki Institute of Physics, PL 64, FIN-00014 Helsingin yliopisto, Finland;
and Ørsted Laboratory, NBIfAFG, University of Copenhagen, Universitetsparken 5, DK-2100 Copenhagen Ø, Denmark

(Received 20 March 2001; published 20 August 2001)

We calculate the light-induced collisional loss of laser-cooled and trapped magnesium atoms for detunings up to 50 atomic linewidths to the red of the ${}^1S_0$-${}^1P_1$ cooling transition. We evaluate loss rate coefficients due to both radiative and nonradiative state-changing mechanisms for temperatures at and below the Doppler-cooling temperature. We solve the Schrödinger equation with a complex potential to represent spontaneous decay, but also give analytic models for various limits. Vibrational structure due to molecular photoassociation is present in the trap loss spectrum. Relatively broad structure due to absorption to the Mg_2 ${}^1\Sigma_u$ state occurs for detunings larger than about ten atomic linewidths. A much sharper structure, especially evident at low temperature, occurs even at smaller detunings due to Mg_2 ${}^1\Pi_g$ absorption, which is weakly allowed due to relativistic retardation corrections to the forbidden dipole transition strength. We also perform model studies for the other alkaline-earth-metal species Ca, Sr, and Ba, and for Yb, and we find similar qualitative behavior as for Mg.

DOI: 10.1103/PhysRevA.64.033425 PACS number(s): 34.50.Rk, 34.10.+x, 32.80.Pj

I. INTRODUCTION

A. Background

Laser cooling and trapping of neutral atoms has recently opened many new research areas in atomic physics. One can cool a gas of neutral atoms in magneto-optical traps (MOT) down to temperatures of 1 mK and below, and obtain densities up to 10^{12} atoms/cm^3. Evaporative cooling methods have allowed the cooling of alkali-metal species to much lower temperatures below 1 μK so that Bose-Einstein condensation (BEC) occurs. Binary atomic collisions play an important role in the physics of cold trapped atomic gases, and have been widely investigated [1]. One of the first cold collisional process to be studied is the heating and loss of trapped atoms that result from tuning laser light to near resonance with the atomic cooling transition [2]. Here we take near resonance, or small detuning, to mean detuning Δ up to 50 natural linewidths to the red of atomic resonance.

Studies of small-detuning trap loss, extensively reviewed by Weiner *et al.* [1], have mainly concentrated on alkali-metal atoms [3], for which it has been very difficult to develop quantitative theoretical models to compare with experiment. This is because alkali-metal atoms have extensive hyperfine structure, and thus the number of collision channels is simply too large for accurate theoretical modeling. It has even been difficult to estimate the relative weight of the different possible loss processes. Although one can develop simplified models, these are difficult to test adequately with complex alkali-metal systems. On the other hand, trap loss photoassociation spectra in alkali-metal systems for large detuning can be modeled quite accurately [4–6]. This is because the underlying molecular physics of alkali-metal dimer molecules is well known, and the spectra are determined by isolated molecular vibrational-rotational levels, for which the photoassociation line shapes can be well characterized even in the presence of a hyperfine structure. Quantitative analyses of such spectra have permitted the determination of scattering lengths for ground-state collisions [1]. These scattering lengths are critical parameters for BEC studies.

Alkaline-earth-metal cooling and trapping have recently been of considerable experimental interest. Trap loss collisions have been studied in a Sr MOT [7], and intercombination line cooling of Sr has resulted in temperatures below 1 μK and raised the prospects of BEC of Sr [8–11]. Ca and Mg are of interest for possible applications as an optical frequency standard [12–16], and photoassociation spectroscopy in a Ca MOT has been reported [17]. Intercombination line cooling has also been reported for Yb [18,19], which we have included in our discussion because of its similarity in structure to alkaline-earth-metal atoms.

Alkaline-earth-metal species provide an excellent testing ground for cold collision theories, especially given the rapidly developing experimental interest in the subject. Since the main isotopes of alkaline-earth-metal atoms have no hyperfine structure, the number of collision channels becomes low enough to allow theoretical calculations even in the small-detuning trap loss regime. Consequently, this paper presents theoretical predictions for small-detuning trap loss spectra in cold and trapped Mg gas in the presence of near-resonant weak laser light tuned near the ${}^1S_0 \rightarrow {}^1P_1$ atomic transition, and discusses the nature of similar processes for Ca, Sr, Ba, and Yb. This work extends our previous paper on

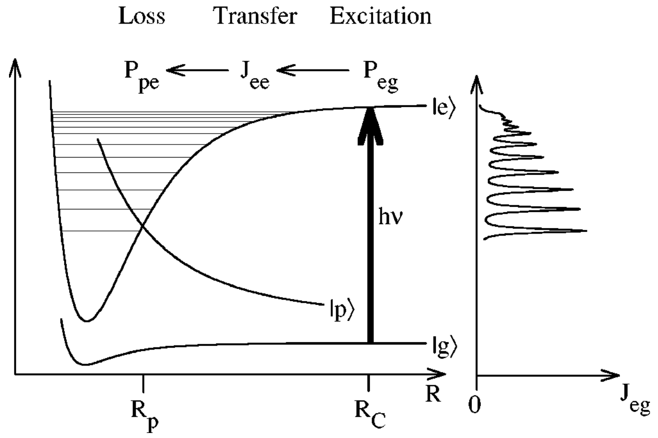

FIG. 1. Schematic representation of trap loss collisions.

the Mg trap loss [20] to other species and lower temperatures, and shows the relation between small-detuning trap loss and photoassociation theory. It is necessary to include spontaneous emission in modeling trap loss collision dynamics because of the long time scale of cold collisions. In addition, relativistic retardation effects play a prominent role at small detunings by allowing transitions to the dipole forbidden $^1\Pi_g$ state, which exhibits resolved vibrational structure, especially at very low temperature. Although we treat the long-range molecular interactions accurately, the potential-energy curves and coupling matrix elements for the dimer molecules in the short-range region of chemical bonding are not sufficiently well known to determine all aspects of trap loss. Therefore, we examine the uncertainties associated with the unknown phases developed in the short-range region of chemical bonding, and we show which features are robust with respect to such uncertainties and which must be measured or later determined from improved theory.

B. Trap loss collisions

Light-induced trap loss takes place as a molecular process. Two colliding cold atoms form a quasimolecule, and their motion can be described in terms of the electronic (Born-Oppenheimer) potentials of the molecular dimer with light-induced transitions between the molecular states. We consider only red detuning, which excites attractive potentials at long range. Such potentials support a number of bound vibrational states.

Figure 1 schematically indicates the nature of the trap loss process in a weak radiation field. An excitation laser with energy $h\nu$ is tuned a few atomic linewidths below the atomic transition energy $h\nu_0$. The ground $|g\rangle$ and excited $|e\rangle$ quasimolecular electronic states are thus coupled resonantly by the laser at some long-range Condon radius R_C, where the photon energy matches the difference between the excited and ground potential-energy curves. The excited state decays to a loss channel $|p\rangle$ due to interactions at short range. The fully quantum-mechanical description in Ref. [21] shows that the overall probability P_{pg} of a trap loss collision can be factored as follows:

$$P_{pg}=P_{pe}J_{eg}. \tag{1}$$

Here J_{eg} represents an excitation-transfer probability which is proportional to the scattering flux that reaches the short-range region near R_p due to long-range excitation near the Condon point followed by propagation on the excited state to the short-range region. P_{pe} represents the probability of a transition from the excited state to the loss channel at short range during a single cycle of oscillation through the short-range region.

Figure 1 indicates the qualitative behavior of the transfer function J_{eg} versus detuning Δ. At very small detuning of a few atomic linewidths J_{eg} becomes very small if there is a high probability of spontaneous emission during transit from the outer to inner regions. At sufficiently large detuning J_{eg} exhibits resonance structure due to the bound vibrational levels in the excited-state potential, where the vibrational period is much shorter than the decay time [22]. This is the domain of photoassociation to individual vibrational levels. Section III C below will show simple analytic formulas for J_{eg} that apply in these two limiting cases of small detuning with fast decay or isolated photoassociation lines. These formulas show how J_{eg} can, in turn, be factored as

$$J_{eg}=J_{ee}P_{eg}, \tag{2}$$

where P_{eg} represents the probability of excitation from the ground to excited state in the outer zone near the Condon point, and J_{ee} represents an excited-state transfer function between the long-range outer excitation zone and the short-range zone. The factorization in Eq. (2) is also schematically indicated in Fig. 1.

Each of the factors in Eqs. (1) and (2) can be affected by unknown phases associated with the short-range molecular physics of the dimer molecules. (1) P_{eg} is sensitive to the asymptotic phase of the ground-state wave function. (2) The vibrational resonance structure in J_{eg} is sensitive to the position and widths of vibrational features. (3) P_{pe} is sensitive to Stückelberg oscillations in short-range curve crossing probabilities. These effects are discussed in detail in Secs. II D and II E. The overall effect of such sensitivities will depend on the temperature and the alkaline-earth-metal species.

There are two possible inner zone loss processes characterized by P_{pe}: the state-change (SC) and radiative-escape (RE) mechanisms, both represented schematically by the loss channel p in Fig. 1. In the SC process the excited state couples to another molecular state near a short-range crossing point R_p, and population transfer between them is possible. The products of the collision emerge on a state that correlates asymptotically with other atomic states of lower energy, such as $^3P+{}^1S$, thereby releasing a large amount of kinetic energy to the separating atoms. In RE the excited-state can decay by spontaneous emission after the atoms have been accelerated towards each other on the excited-state potential. The ground-state atoms then separate with this gain in kinetic energy. If enough kinetic energy has been gained to exceed the trap depth, this is a loss process (early decay after insufficient acceleration only leads to radiative heating). Here R_p represents the distance at which the atoms have received sufficient acceleration to be lost from the trap. Any emission with $R<R_p$ leads to trap loss.

In this paper we use the fully quantum complex potential method of Ref. [21] and we do not resort to semiclassical methods (with one exception), although semiclassical concepts are often useful for interpretation. Our quantum methods are fully capable of describing the *s*-wave limit and the quantum threshold properties of the extremely low collision energies near or below the critical temperature for BEC. We describe the spontaneous-emission processes with a complex potential, and solve the corresponding time-independent multichannel Schrödinger equation in the molecular electronic state basis. This takes any vibrational state structure into account automatically without the need to calculate wave functions or Franck-Condon factors, but limits our study to weak laser fields only, where only a single photon is exchanged with the field. Typical cooling lasers are strong and detuned only a few linewidths. By alternating with a weaker probe laser one can access the particular range of detuning and intensity that we study. Future studies are needed to address the effects of strong laser fields and the consequent revision of our results due to saturation and power broadening [23,24].

We also include rotational states in our model, which for the molecular ground state correspond to the partial waves of a standard scattering problem (angular momentum quantum number l). The symmetry of spinless alkaline-earth-metal dimers permits only even partial waves. It should be pointed out that for near-resonant light the Condon point is at relatively large distances. This means that although the collision energy is low, one needs to go to relatively large l before the ground-state centrifugal barrier stops the quasimolecule from reaching R_C. We correct here some mistakes that we discovered in the sum over partial waves in Ref. [20].

The probe laser can be tuned over a wide range from a few to many atomic linewidths. For sufficiently large detuning the rotational structure becomes sharp, and it should be possible to resolve the vibrational and rotational states. However, even at 27 GHz detuning, rotational features in the Ca_2 $^1\Sigma_g \rightarrow {}^1\Sigma_u$ photoassociation spectrum are only partially resolved [17]. Photoassociation studies can yield precise information on the molecular potentials. Also, the photoassociation line shapes are sensitive to the near-threshold ground-state wave function, especially if it has nodes in the region swept by the detuning-dependent Condon point. The sensitivity to the *s*-wave scattering length is examined in Secs. II D and IV B. Analysis of photoassociation spectra would hopefully lead to a value of the unknown *s*-wave scattering length for Mg or other alkaline-earth-metal species, and consequently determine whether a stable Bose-Einstein condensate is possible.

In this paper we present the calculated estimates for trap loss rate coefficients in Mg at temperatures around and below the Doppler temperature. The contributions from different mechanisms and states are identified and compared. We also calculate predictions for other alkaline-earth-metal atoms and Yb by combining the appropriate atomic properties with model molecular potentials. Section II presents in detail the atomic data, molecular potentials, and laser couplings used for Mg and other alkaline-earth-metal atoms. Section III describes our theoretical approach. The results for Mg are given in Sec. IV and for the other atoms (Sr, Ca, Ba, Yb) in Sec. V. Finally, we present some conclusions in Sec. VI.

II. THE MOLECULAR PHYSICS OF ALKALINE-EARTH-METAL DIMER MOLECULES

A. Alkaline-earth atomic structure

Table I gives the basic atomic data for the alkaline-earth-metal atoms and Yb, which has an electronic structure similar to the group-II elements. The major isotopes have no hyperfine structure, except for Be. Alkaline-earth-metal atoms have a $^1S_0$ ground state, and excited $^1P_1$ and $^3P_1$ states that are optically connected to the ground state, the latter weakly. Figure 2 sketches the energy levels of the group-II atoms. The $^{1,3}P$ first excited states are the most important for laser cooling. The $^{1,3}D$ states shift downwards as the atomic number increases. For Mg the $^{1,3}D$ states are above the $^{1,3}P$ states. For Ca and Sr they are between the ^3P and the ^1P states, and for Ba the $^{1,3}D$ states are below the $^{1,3}P$ states. In laser cooling one uses typically the $^1S_0$-$^1P_1$ transition, which is the situation studied in this paper. For Mg this requires a UV laser source, and for the heavier elements it requires repumping to recycle atoms that decay to lower levels. The weak $^1S_0$-$^3P_1$ intercombination transition has a very narrow linewidth, and is within the optical range. Thus alkaline-earth-metal atoms are good candidates for optical atomic clocks when cooled to low temperatures. For clock applications we need to understand their laser cooling properties, including the magnitude and nature of laser-induced collisional trap loss.

Beryllium is not likely to be a serious candidate for laser cooling. It is toxic, has a very short-wavelength cooling transition, and the intercombination "clock" transition is so weak as to be effectively forbidden. Therefore, we will not consider Be in the rest of this paper.

Because of the lack of hyperfine structure, the basic laser cooling mechanism for alkaline-earth-metal atoms is Doppler cooling, for which the temperature limit T_D, defined in the caption of Table I, is set by the linewidth Γ_{at} of the cooling transition (widths in this paper are expressed in energy units, so that the decay rate is $\Gamma_{\mathrm{at}}/\hbar$). The lifetime of the alkaline-earth-metal $^1P_1$ state is between 1.8 and 8.4 ns, giving a Doppler-cooling limit between 2.1 and 0.45 mK for the elements in Table I. On the other hand, the $^3P_1$ state has a long lifetime with Doppler-cooling limits in the nano-Kelvin range. This can be compared to the photon recoil limit T_R, defined in the caption of Table I; Table I shows that T_R is between 0.2 and 4 μK. Thus the recoil limit is above the intercombination line Doppler-cooling limit for Mg and Ca, nearly coincident with it for Sr, and below it for Ba and Yb.

Although Sisyphus cooling and magnetic trapping is not available for $^1S_0$ atoms as it is for alkali-metal atoms, intercombination line cooling is possible for some group-II species. This has been used to cool Sr to ~ 400 nK with relatively high phase space density >0.1 [8,9]. If combined with far off-resonant optical traps and evaporative cooling it may

TABLE I. Atomic data for major isotopes of group-II elements and Yb without hyperfine structure (natural abundance shown). Most data are derived from [25]. The lifetime τ for $^1P_1$ is taken to be the inverse of the $^1P_1$-$^1S_0$ spontaneous-emission rate $\Gamma_{\rm at}/\hbar$, thus neglecting weak transitions to other states for Ba and Yb. The ^3P lifetimes are from several sources [26]. The linewidth in frequency units is $\Gamma_{\rm at}/h = (2\pi\tau)^{-1}$. The wavelengths λ and fine-structure splittings for Sr and Ba are taken from [27]. The Doppler temperature is defined as $T_D = \Gamma_{at}/(2k_B)$. We take the recoil temperature to be $T_R = (\hbar^2)/(m\lambda\!\!\!^{-2} k_B)$, where $\lambda\!\!\!^{-} = \lambda/2\pi$ and m is the atomic mass. The dipole moment is $d_0 = \sqrt{3\Gamma_{\rm at}\lambda\!\!\!^{-3}/4}$ (in a.u.). The atomic units for dipole moment, length, and energy are $ea_0 = 8.4783\times10^{-30}$ Cm, $a_0 = 0.0529177$ nm, and $e^2/(4\pi\epsilon_0 a_0) = 4.3597482\times10^{-18}$ J, respectively.

	Be	Mg	Ca	Sr	Ba	Yb
Major isotopes without hyperfine structure (abundance)	^{9}Be (100%)	^{24}Mg (78.99%) ^{26}Mg (11.01%)	^{40}Ca (96.94%)	^{88}Sr (82.58%) ^{86}Sr (9.86%)	^{138}Ba (71.70%)	^{174}Yb (31.8%) ^{172}Yb (21.9%)
τ						
$^1P_1$ (ns)	1.80	2.02	4.59	4.98	8.40	5.68
$^3P_1$ (ms)		5.1	0.48	0.021	0.0014	0.00088
$\Gamma_{\rm at}/h$						
$^1P_1$ (MHz)	88.5	78.8	34.7	32.0	18.9	28.0
$^3P_1$ (kHz)		0.031	0.33	7.5	120	181
Doppler-cooling limit						
$^1P_1$ (mK)	2.1	1.9	0.83	0.77	0.45	0.67
$^3P_1$ (nK)		0.75	8.0	179	2.8×10^3	4.4×10^3
Recoil limit						
$^1P_1$ (μK)	39	9.8	2.7	1.0	0.45	0.69
$^3P_1$ (μK)		3.8	1.1	0.46	0.22	0.36
d_0 (a.u.)						
$^1S_0-{}^1P_1$	1.89	2.38	2.85	3.11	3.16	2.35
λ (nm)						
$^1S_0-{}^1P_1$	234.861	285.21261	422.6728	460.733	553.548	398.799
$\lambda\!\!\!^{-} = \lambda/(2\pi)$ (a_0)						
$^1S_0-{}^1P_1$	706.4	857.8	1271.2	1385.7	1664.9	1199.4
FS splitting						
$^3P_2-{}^3P_0$ (a.u.)	1.36×10^{-5}	2.77×10^{-4}	7.20×10^{-4}	2.65×10^{-3}	5.69×10^{-3}	1.10×10^{-2}

become possible to obtain Bose-Einstein condensation with optical methods alone.

B. Alkaline-earth-metal dimer molecular structure

Figure 3 shows the lowest electronic potentials for Mg_2 [28]. There are only two states with attractive long-range potentials correlating with $^1P_1 + {}^1S_0$ that can be resonantly coupled to the ground state by laser light, namely $^1\Sigma_u^+$ and $^1\Pi_g$. Both states offer the possibility for the SC and RE mechanisms. When comparing Figs. 2 and 3 one can see that Mg is special. For other alkaline-earth-metal atoms the molecular state picture is further complicated by the atomic D states below the $^1P_1$ state. This increases the number of molecular states and thus the number of energetically available exit channels. The small number of molecular states is one reason we have chosen Mg as the basis for our studies. Theoretical calculations require precise information about the molecular potentials and couplings over a wide range of

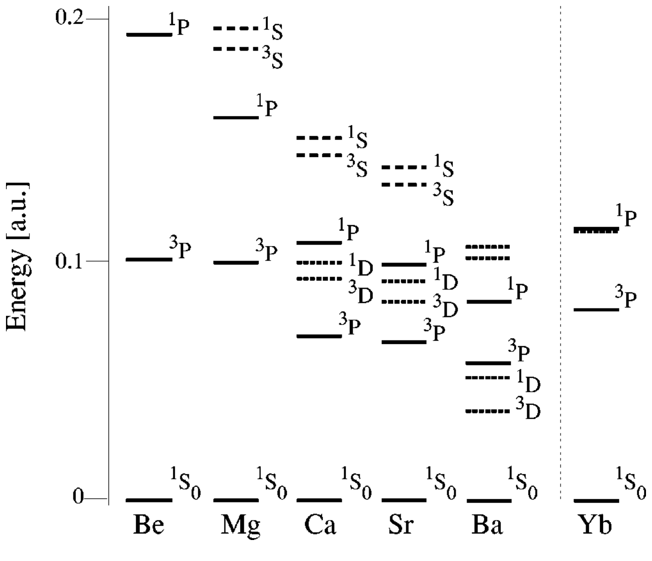

FIG. 2. Energy levels of group-II atoms and Yb.

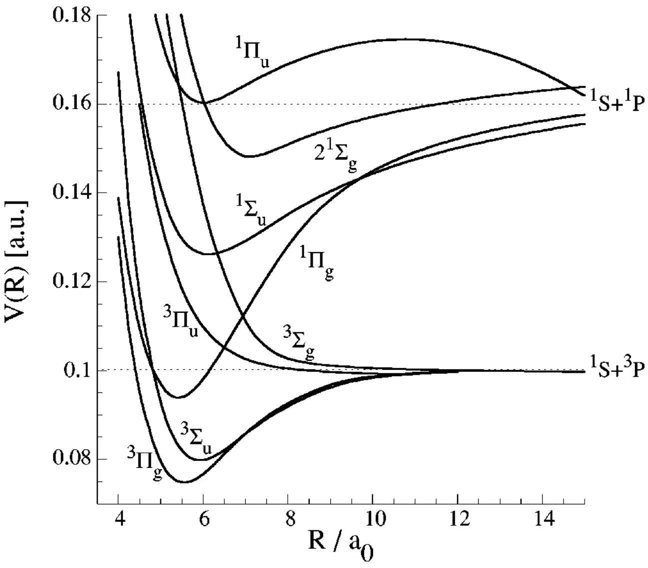

FIG. 3. The molecular states of Mg_2 in atomic units corresponding to the asymptotic atomic states $^1S_0 + ^1P_1$ and $^1S_0 + ^3P_{0,1,2}$ [28]; the zero of energy is at the ground state $^1S_0 + ^1S_0$ asymptote. There are four states correlating with each asymptote, of which two are attractive and two are repulsive at large R, where the system is expected to be resonant with the laser field.

interatomic distance. *Ab initio* calculations of ground and excited molecular potentials are also available for Sr [29] and Ba [30].

While working on the manuscript we received new *ab initio* data on Mg_2 from E. Czuchaj, including both improved potential curves and spin-orbit couplings [31]. Although the new data differ to some extent from the results of Stevens and Krauss [28] because of improved calculations of electron correlation effects, we do not expect that use of the new data would lead to any strong modification of our basic results, which should be viewed as qualitative model calculations for the reasons to be discussed in the following sections.

The linewidth of the excited $^1\Sigma_u$ state depends on the interatomic distance R with a magnitude on the order of twice the atomic linewidth. Thus the vibrational levels of the $^1\Sigma_u$ state near the $^1S + ^1P$ dissociation limit overlap strongly, and one does not expect to resolve them. One interesting point is that the dipole-forbidden $^1\Pi_g$-$^1\Sigma_g$ transition becomes allowed at large R due to retardation corrections. This means that the $^1\Pi_g$ state can be excited at R_C, but the spontaneous-emission probability goes down quickly as R decreases. Consequently, $^1\Pi_g$ vibrational states near the dissociation limit have narrow emission linewidths. Thus the assumption that the vibrational states overlap strongly and cannot be resolved at detunings of a few linewidths is not necessarily valid. One must determine if resolvable features persist when one sums over all rotational states and partial waves, and takes the energy average over a thermal distribution. We show that one can indeed see vibrational structure, especially if the temperature is well below the $^1S_0$-$^1P_1$ Doppler limit. As mentioned above, this is by no means impossible, if one does the cooling using the $^1S_0$-$^3P_1$ transition.

TABLE II. Condon points in scaled distance for selected detunings.

Detuning Δ	$u_C(^1\Sigma_u^+)$	$u_C(^1\Pi_g)$
$\Gamma_{\rm at}$	1.32	0.849
$5\Gamma_{\rm at}$	0.716	0.511
$10\Gamma_{\rm at}$	0.555	0.411
$30\Gamma_{\rm at}$	0.376	0.288

C. Long-range properties of states correlating with $^1P_1 + ^1S_0$ atoms

There are four molecular states correlating with $^1P_1 + ^1S_0$ atoms: two long-range attractive states, $^1\Sigma_u^+$ and $^1\Pi_g$, and two long-range repulsive states, $^1\Sigma_g^+$ and $^1\Pi_u$. Here long-range means that R is large compared to the short-range region of chemical bonding and van der Waals interactions shown in Fig. 3 so that the potential is determined by the first-order dipole-dipole interaction with $C_3 = \mp 2d_0^2$ and $\mp d_0^2$ for the $^1\Sigma$ and $^1\Pi$ states, respectively. Here d_0 is the z component of the atomic transition dipole matrix element, which is related to the atomic linewidth $\Gamma_{\rm at}$ and the reduced wavelength of the $^1S_0$-$^1P_1$ transition ($\bar{\lambda} = \lambda/2\pi$) by $d_0^2 = 3\bar{\lambda}^3\Gamma_{\rm at}/4$. The exact long-range (lr) potentials including relativistic retardation corrections are [32]

$$V_{\rm lr}(u;^1\Sigma_u^+) = -\frac{3\Gamma_{\rm at}}{2u^3}[\cos(u) + u\sin(u)], \tag{3}$$

$$V_{\rm lr}(u;^1\Pi_g) = -\frac{3\Gamma_{\rm at}}{4u^3}[\cos(u) + u\sin(u) - u^2\cos(u)],$$

where $u = R/\bar{\lambda}$ is the scaled distance. The molecular linewidths with relativistic retardation corrections are [32]

$$\Gamma(u;^1\Sigma_u^+) = \Gamma_{\rm at}\left\{1 - \frac{3}{u^3}[u\cos(u) - \sin(u)]\right\}, \tag{4}$$

$$\Gamma(u;^1\Pi_g) = \Gamma_{\rm at}\left\{1 - \frac{3}{2u^3}[u\cos(u) - (1-u^2)\sin(u)]\right\}.$$

In the region with $R < \bar{\lambda}$ the potentials vary as $1/u^3$, and $\Gamma(^1\Sigma_u^+)$ and $\Gamma(^1\Pi_g)$, respectively, vary as $2\Gamma_{\rm at}$ and $\Gamma_{\rm at}u^2/5$.

The very long-range excited-state potentials result in large Condon points for excitation of the attractive states. If the laser detuning relative to the atomic transition is expressed in units of $\Gamma_{\rm at}$ and the distance in units of $\bar{\lambda}$, the scaled Condon point (u_C) for the ground-excited state transition becomes independent of atomic species. Table II shows u_C for several detunings Δ, where we define red detuning to be positive. For Mg at $\Delta = \Gamma_{\rm at}$ we have $R_C(^1\Sigma_u^+) = 1132a_0$ and $R_C(^1\Pi_g) = 728a_0$.

The attractive potentials support a series of vibrational levels leading up to the dissociation limit. Assuming a potential with a long-range form $-C_3/R^3$ gives the binding energy of vibrational level v [33]:

$$\varepsilon_v^{1/3} = \left(\frac{\pi}{2a_3}\right)^2 \frac{\hbar^2}{2\mu C_3^{2/3}}(v - v_D)^2, \tag{5}$$

where $a_3 = (\sqrt{\pi}/2)\Gamma(5/6)/\Gamma(4/3) = 1.120\,251$, v_D is the vibrational quantum number at the dissociation limit (v_D is generally nonintegral), and μ is the reduced mass. The vibrational spacing function, which we need later, is

$$\frac{\partial \varepsilon_v}{\partial v} = h\nu_v = \frac{3\pi}{a_3}\left(\frac{\hbar^2}{2\mu C_3^{2/3}}\right)^{1/2} \varepsilon_v^{5/6}, \tag{6}$$

where $h\nu_v$ is the vibrational frequency.

D. Ground state

The ground-state van der Waals potential varies at long range as R^{-6} and is essentially flat for the range of Condon points we consider. The energy-normalized ground-state scattering wave function for collisional momentum $\hbar k_\infty$ and partial wave l has the long-range form

$$\Psi(R,l,k_\infty) = \left(\frac{2\mu}{\pi\hbar^2 k_\infty}\right)^{\frac{1}{2}} \sin\left[k_\infty R - \frac{\pi}{2}l + \eta_l(k_\infty)\right]. \tag{7}$$

We define the collisional energy as $\varepsilon = \hbar^2 k_\infty^2/(2\mu)$. The short-range potentials are not sufficiently well-known for alkaline-earth-metal dimers to determine accurately the scattering phase shifts $\eta_l(k_\infty)$. Therefore, our calculations will have to be model calculations. However, we test the sensitivity of our trap loss spectra to the unknown phases, and show that this is not a serious limitation. There are two reasons for this. One is that the ground-state potential is flat in the long-range region, and the amplitude of $\Psi(R,l,k_\infty)$ has its asymptotic value in Eq. (7) independent of R as long as $R > x_0 = \frac{1}{2}(2\mu C_6/\hbar^2)^{1/4}$ [34,35]; the use of x_0 (or a closely related length) as an appropriate length scale for van der Waals potentials is described in the Appendix of Ref. [6]. The condition $R_C \gg x_0$ is easily satisfied in our case. Second, at the Doppler limit T_D for ${}^1S_0 \rightarrow {}^1P_1$ cooling, a number of partial waves l contribute to trap loss in our detuning range (1–$50\ \Gamma_{\rm at}$). We demonstrate in Sec. IV A that a sum over l eliminates the dependence on the short-range potential.

Our trap loss spectra for *s*-wave scattering at the low temperatures available via intercombination line cooling will be sensitive to the actual scattering length A_0 of the ground ${}^1\Sigma_g^+$ potential. However, we demonstrate a simple scaling relationship that will allow our low T *s*-wave results to be scaled to any value of the scattering length. We may expect that the ${}^1\Sigma_g^+$ scattering length can be determined from one or two-color photoassociation spectra, as has been done for alkali-metal species [1]. However, such an analysis will require an accurate C_6 coefficient and for optimum results needs a reasonably accurate short-range potential as well.

E. Excited-state short-range potentials

Trap loss spectra depend strongly on the excited-state short-range potential structure in three ways.

(1) The curve crossings leading to SC trap loss occur at short range, and determine P_{pe}. In a Landau-Zener interpretation,

$$P_{pe}(J') = 4e^{-2\pi\Lambda}(1 - e^{-2\pi\Lambda})\sin^2(\beta_{J'}), \tag{8}$$

where $\Lambda = |V_{pe}(R_p)|^2/(\hbar v_p D_p)$ and J' designates excited-state total angular momentum (see Sec. II F). Here $V_{pe}(R_p)$, v_p, D_p are the respective coupling matrix element, speed, and slope difference at the R_p crossing, and $\beta_{J'}$ is a semiclassical phase angle [36]:

$$\beta_{J'} = \int_{R_{0e}}^{R_p} k_e(R,J')dR - \int_{R_{0p}}^{R_p} k_p(R,J')dR + \frac{\pi}{4}, \tag{9}$$

where R_{0i} and $\hbar k_i(R,J')$ are the respective inner classical turning point at zero energy and local momentum for state $i = e$ or p. The attractive singlet potentials may have one or more crossings with repulsive potentials from lower-lying states, e.g., those correlating to ${}^3P + {}^1S$. Thus the number, positions of crossings, and the coupling between states with crossing potentials are important for the magnitude of P_{pe}. Although we can make reasonable estimates for Λ, the phase angle $\beta_{J'}$ is sensitive to details of the potentials and can only be calculated accurately if very accurate potentials are available [37].

(2) The vibrational structure in the trap loss spectra depends on both short- and long-range potentials. The spacing between the vibrational levels given by Eq. (6) depends only on the long-range potentials, but the exact positions of the levels in Eq. (5) are determined by the short-range potentials in the region of chemical bonding (through the v_D parameter). Thus, the magnitude of the vibrational spacings in our model calculations will be correct, whereas the actual positions can only be determined by measurement.

(3) The short-range SC process also contributes to the width of vibrational features in the trap loss spectra [38]. Depending on species, temperature, and detuning, the widths may be primarily determined by natural or thermal broadening or by the predissociation decay rate related to P_{pe}. However, we are able to place approximate bounds on the magnitude of P_{pe}. Sections III C, IV, and V discuss the contributions to feature widths and show that natural and thermal broadening tends to be dominant at small detuning, whereas SC broadening may become dominant at large detuning.

The available data on short-range potentials varies among the group-II elements. *Ab initio* potentials are available for Mg [28,31]. The structure of the molecular potentials is fairly simple because only states correlating to ${}^1P + {}^1S$ (four states) and ${}^3P + {}^1S$ atoms (four states) are present (see Fig. 3) and the potentials provide qualitative data for possible SC mechanisms. On the other hand, Ca, Sr, and Ba have a very complex short-range structure, because of large fine-structure splittings in the triplet states, and the states correlating to ${}^1D + {}^1S$ and ${}^3D + {}^1S$ coming into play. For example, Boutassetta *et al.* [29] and Allouche *et al.* [30] calculated the short-range potentials for Sr and Ba, respectively, but the large number of states (e.g., 38 states for Ba) makes it excessively complicated to treat the short-range SC mechanism even qualitatively.

The coupling between the singlet and triplet states at short-range is due to spin-orbit couplings. The exact magnitude of the couplings is unknown for all group-II elements, but can be estimated using Table A1 of Ref. [39], which relates the coupling matrix elements to the ${}^3P_2 - {}^3P_0$ fine-structure splitting. This approximation ignores any R dependence of the spin-orbit matrix elements due to chemical bonding. The fine-structure splitting of the ${}^3P$ state increases with atomic number (see Table I).

We have opted for Mg as a model system, because short-range potentials are available. Each singlet state with attractive potential couples to only one triplet state in the inner zone. Thus the SC trap loss problem for Mg decouples into two three-state calculations, one for the ${}^1\Sigma_u^+$ and one for the ${}^1\Pi_g$ excited state. For Mg we provide qualitatively correct SC trap loss spectra and even give some quantitative estimates.

In the case of the other group-II elements and Yb, we treat their complicated inner zone physics as one effective crossing, that is, we use three-state calculations based on the Mg model, and explore the effects of mass, radiative properties, and coupling strength (size of spin-orbit splitting) in these model calculations. Thus we do not use the *ab initio* potentials of Refs. [29,30] discussed in the paragraph above, because even if we were to include all the curves, there would still be uncertainties associated with unknown phases and unknown coupling matrix elements. Rather, our goal is to indicate qualitative differences in magnitude and spectral shapes among the various species. We trust that these will be helpful in providing guidance for future experimental and theoretical studies of these systems. As we discuss in Sec. III B, our calculation of the excitation-transfer coefficient κ will be to a large extent independent of details of the complicated short-range molecular physics and curve crossings.

F. Molecular rotational structure and coupling to the laser field

The full three-dimensional treatment of the collision of a ${}^1S$ atom coupled to a ${}^1P$ atom by a light field is worked out in Ref. [40]. We adapt this treatment to our simplified model with molecular Hund's case (a) transitions between two molecular states with the usual rotational branch structure. The angular momentum J'' in the ground state can only be that of molecular axis rotation, $J''=l''$ with projection m'' on a space-fixed axis. The excited rotational levels in a Hund's case (a) molecular basis for a ${}^1\Sigma_u^+$ or ${}^1\Pi_g$ state do not have mechanical rotation l' as a good quantum number but instead the total angular momentum J' with space projection M'. The three possible transition branches have $J'=l''+B$, where the branch labels P, Q, and R, respectively, designate the cases $B=-1$, 0, and 1. The quasimolecule ground state can couple to the ${}^1\Sigma_u^+$ state only by P and R branches, but to the ${}^1\Pi_g$ state by P, Q, and R branches. All potentials have a centrifugal term added, $n(n+1)/(2\mu R^2)$, depending on ground state $n=l''$ or excited states $n=J'=l''+B$.

TABLE III. The rotational line strength factors $\sqrt{2l''+1}\ \alpha_{A,B,l''}$.

State A	Branch B	$l''=0$ (s wave)	$l''\neq 0$
Σ	P	0	$\sqrt{l''/3}$
Σ	R	$\sqrt{2/3}$	$\sqrt{(l''+1)/3}$
Π	P	0	$\sqrt{(l''-1)/3}$
Π	Q	0	$\sqrt{(2l''+1)/3}$
Π	R	$2/\sqrt{3}$	$\sqrt{(l''+2)/3}$

The radiative coupling terms are

$$V_{A,B,l'',m'',q}(u)=\left(\frac{2\pi I}{c}\right)^{1/2}\langle A,J'M'|\hat{e}_q\cdot\vec{d}|l''m''\rangle, \quad (10)$$

where $A={}^1\Sigma_u^+$ or ${}^1\Pi_g$ labels the excited state, I is light intensity, $\vec{d}$ is the laboratory frame dipole operator, $\hat{e}_q$ is the polarization vector of light with polarization $q=0,\pm 1$, and M', m'' are laboratory frame angular momentum projection quantum numbers. In our weak-field case, where transition probabilities are linear in $|V_{A,B,l'',m''(u),q}|^2$, we can define an m''-averaged radiative coupling matrix element (the sum over m'' eliminates the dependence on q):

$$\begin{aligned}V_{eg,A}(u,l'',B,I)&=\left(\frac{1}{2l''+1}\sum_{m''=-l''}^{l''}\left|V_{A,B,l'',m'',q}(u)\right|^2\right)^{1/2}\\&=\left(\frac{2\pi I}{c}\right)^{1/2}\alpha_{A,B,l''}d_A(u)\\&=2.669\times 10^{-9}\alpha_{A,B,l''}\sqrt{I(\mathrm{W/cm^2})}\,d_A(u).\end{aligned} \quad (11)$$

in atomic units. The molecular electronic transition dipole moment d_A is

$$d_A(u)(\mathrm{a.u.})=\sqrt{\frac{3\lambdabar\ (\mathrm{a.u.})^3}{4}\Gamma_A(u)(\mathrm{a.u.})}, \quad (12)$$

where $\Gamma_A(u)$ is the molecular linewidth of the excited state as in Eq. (4). The factors $\sqrt{2l''+1}\,\alpha_{A,B,l''}$ are given in Table III.

G. Model potentials for Mg

Our results are not sensitive to the detailed form of the ground-state potential, for the reasons given in Sec. II D. Thus, we model the ground-state potential by a Lennard-Jones 6-12 form

$$V_g(u)=4\epsilon\left[\left(\frac{\sigma}{\lambdabar u}\right)^{12}-\left(\frac{\sigma}{\lambdabar u}\right)^{6}\right]. \quad (13)$$

For Mg we model the ground-state potential from [28] with a well depth of $\epsilon=0.002\,825$ a.u. and an inner turning point of $\sigma=6.23a_0$. This potential has a scattering length of $-95a_0$ for the ^{24}Mg reduced mass of 23.985042/2 atomic mass units. The scattering length A_0 is determined from the $k \rightarrow 0$ behavior of the *s*-wave phase shift: $\eta_0 = -k_\infty A_0$.

Since the excited *ab initio* potentials of Ref. [28] do not permit a quantitative calculation of spectroscopic accuracy, for the reasons given in Sec. II E, the specific forms of the short-range (sr) excited-state potentials are not important for our purposes of modeling the qualitative structure and magnitude of the collisional loss. However, it is important to retain the correct long-range form. Therefore, for simplicity in the calculations and because we want to model the other alkaline-earth systems to explore the effect of different C_3, Γ_{at}, $\bar{\lambda}$, and mass, we have modeled the *ab initio* potentials with Lennard-Jones 3-6 potentials keeping the long-range form fixed to its known C_3 value given in Eq. (3),

$$V_{\mathrm{sr}}(u) = 4\epsilon\left[\left(\frac{\sigma}{\bar{\lambda}u}\right)^6 - \left(\frac{\sigma}{\bar{\lambda}u}\right)^3\right]. \tag{14}$$

We have two fitting parameters ϵ and σ, and three given values: well depth of the *ab initio* potential (the depth of the model potential is ϵ), the position of minimum u_{min} and $C_3(^1\Sigma_u^+) = -2d_0^2$ or $C_3(^1\Pi_g) = -d_0^2$. Because we want to fix the long-range potential C_3 we cannot fit u_{min} and the well depth at the same time and have chosen the latter:

$$V_e(u;{}^1\Sigma_u^+) = 4\epsilon(\Sigma)\left(\frac{\sigma(\Sigma)}{\bar{\lambda}u}\right)^6 - \frac{2d_0^2}{\bar{\lambda}^3 u^3}[\cos(u) + u\sin(u)], \tag{15}$$

$$V_e(u;{}^1\Pi_g) = 4\epsilon(\Pi)\left(\frac{\sigma(\Pi)}{\bar{\lambda}u}\right)^6 - \frac{d_0^2}{\bar{\lambda}^3 u^3}[\cos(u) + u\sin(u) - u^2\cos(u)], \tag{16}$$

where

$$\epsilon(\Sigma) = 0.0347 \;\; \text{a.u.}, \quad \sigma(\Sigma) = 4.339a_0,$$

$$\epsilon(\Pi) = 0.0681 \;\; \text{a.u.}, \quad \sigma(\Pi) = 2.751a_0.$$

The well minima are $\bar{\lambda}u_{\mathrm{min}} = 5.5a_0$ and $3.5a_0$ for $^1\Sigma_u^+$ and $^1\Pi_g$, respectively, compared to the *ab initio* values $\bar{\lambda}u_{\mathrm{min}} = 6.1a_0$ and $5.4a_0$.

Both excited states have a SC mechanism in the short-range region with coupling to a triplet state. The triplet states are purely repulsive, and modeled with

$$V_{p,A}(u) = \frac{C_6}{\bar{\lambda}^6 u^6} + V_\infty, \tag{17}$$

where $A = {}^3\Sigma_u$ or $^3\Pi_g$ labels the molecular state, and $V_\infty = -0.0601$ a.u.

The SC from $^1\Sigma_u^+$ to $^3\Pi_u$ takes place around the inner turning point of the $^1\Sigma_u^+$ potential well. We have chosen $C_6 = 392$ a.u. for the model of the $^3\Pi_u$ state.

The SC from $^1\Pi_g$ to $^3\Sigma_g$ takes place about $1.5a_0$ outside and 0.019 a.u. above the minimum of the $^1\Pi_g$ state potential well. With $C_6 = 81$ a.u. we have a model of the crossing where the corresponding values are $1.0a_0$ and 0.019 a.u. The difference in slope of the crossing potentials is 0.030 a.u. for the *ab initio* potentials and 0.037 a.u. for the model.

The coupling between the crossing states are approximated using Table A1 of Ref. [39]. The $^1\Sigma_u^+$-$^3\Pi_u$ and $^1\Pi_g$-$^3\Sigma_g^+$ matrix elements are $\zeta/\sqrt{2}$ and $\zeta/2$, respectively, where $\zeta = 1.84 \times 10^{-4}$ a.u. is 2/3 of the atomic $^3P_2$-$^3P_0$ splitting. For example, we estimate an upper bound ($\sin^2\beta_{J'} = 1$) to the Landau-Zener version of P_{pe} in Eq. (8) for the $^1\Pi_g$-$^3\Sigma_g$ crossing to be 2.6×10^{-3} for the model potentials and 2.8×10^{-3} estimated from the *ab initio* potentials. This upper bound is consistent with the calculated P_{pe} as a function of J' from our complex potential calculation described below.

Since we will use a semiclassical method to determine the P_{pe} factor for the RE process via the $^1\Sigma_u^+$ state (see Sec. III D below), we do not need an explicit probe channel for RE. However, we introduce a probe channel to simulate RE in order to show that the same J_{eg} factor in Eq. (1) applies for both SC and RE processes, irrespective of the choice of the short-range R_p. Since we may take any form we like for a RE probe state, we use a probe state potential which crosses the excited state at a distance u_p, where the kinetic energy gained by the collision pair is 1 K, corresponding to a trap depth of 0.5 K. The RE probe potential has a repulsive inner wall

$$V_{\mathrm{RE,probe}}(u) = \frac{C_{12}}{(\bar{\lambda}u)^{12}} - V_{\mathrm{kin,RE},\infty}, \tag{18}$$

where $V_{\mathrm{kin,RE},\infty} = 3.17 \times 10^{-6}$ a.u. and $C_{12} = 5 \times 10^6$ a.u. No rotational term is included in this probe channel. The same probe state potential is used for all collision energies, which are small (mK range and below) compared to the 1 K kinetic energy at u_p. The coupling between the excited state and the probe state is chosen to be weak: 10^{-9} a.u.

H. Model potentials for Ca, Sr, Ba, and Yb

Since the different ground-state values of C_6 and inner potential shape make no difference for these model studies, for the reasons given in Sec. II G, we take the same ground-state Lennard-Jones 6-12 potential, Eq. (13), as in the Mg case to model the other alkaline-earth-metal ground states, and only change the reduced mass. This procedure yields respective model scattering lengths of $67a_0$, $-65a_0$, $-41a_0$, and $97a_0$ for ^{40}Ca, ^{88}Sr, ^{138}Ba, and ^{174}Yb. Thus, $|A_0| \ll R_C$ in all model cases.

The long range of the excited-state potentials for Ca, Sr, Ba, and Yb is still exact, using the data from Table I with the form in Eq. (3). Due to the lack of accurate excited-state short-range molecular potentials and because of their more complicated structure, we model the trap loss for Ca, Sr, Ba, and Yb by scaling the potentials from the Mg model Eqs. (15) and (16). The well depth ϵ of the $^1\Sigma_u^+$ and $^1\Pi_g$ potentials are scaled by the size of the singlet-triplet states splitting compared to that splitting in Mg, e.g.,

$$\epsilon_{\mathrm{Ca}}=\epsilon_{\mathrm{Mg}}\frac{E({}^1P,\mathrm{Ca})-E({}^3P,\mathrm{Ca})}{E({}^1P,\mathrm{Mg})-E({}^3P,\mathrm{Mg})}. \tag{19}$$

The short-range structure is treated as one effective crossing. The probe states are qualitatively like those in the Mg model. The position (in energy) of the crossing between the ${}^1\Pi_g$ and probe state potentials is scaled as above. The ${}^1\Sigma_u^+$ and probe state potentials come very close at the inner wall of the ${}^1\Sigma_u^+$ potential around the classical turning point $V_e(u)=\varepsilon$.

The spin-orbit coupling constant ζ scales with the spin-orbit splitting of the ^{3}P atomic states. We use the same definition of the matrix elements as for Mg. The Landau-Zener adiabaticity parameter $2\pi\Lambda$ in Eq. (8) for Ba and Yb is larger than unity, leading to a modified shape of the short-range adiabatic potentials and very small $P_{pe,\mathrm{SC}}$. Thus for Ba the ${}^1\Sigma_u^+$-probe state coupling and for Yb the ${}^1\Pi_g$ and the ${}^1\Sigma_u^+$-probe state couplings have been reduced by about a factor 5 to obtain values of $P_{pe,\mathrm{SC}}$ close to unity, in order to test the limit of very strong broadening of the vibrational structure. We believe this limit is physically more realistic. The variety of crossings in these systems might lead to a strong SC process.

III. COMPLEX POTENTIAL CLOSE-COUPLED CALCULATIONS

A. Description of method

The weak-field approximation assumed in this study allows us to apply a complex potential method [21,41], since reexcitation of any decayed quasimolecular population can be ignored. Furthermore, the weak field only couples each ground-state partial wave to at most 3 rotational states of the ${}^1\Sigma_u$ or ${}^1\Pi_g$ state through the *P*, *Q*, or *R* branches. However, in the weak field the excited-state rotational states do not couple further to other ground-state partial waves. Therefore we can ignore any partial wave ladder climbing. Thus, for each trap loss mechanism we have three dressed states: a ground state *g*, an excited state *e*, and a probe state *p*. We solve the three-channel, time-independent radial Schrödinger equation for ground-state collision energy ε, partial wave $l=l''$, for each transition branch *B* and for a given intensity *I*

$$\frac{d^2}{dR^2}\boldsymbol{\phi}(\varepsilon,R)+\frac{2\mu}{\hbar^2}[\varepsilon\mathbf{1}-\mathbf{V}(R,l,B,\Delta,I)]\boldsymbol{\phi}(\varepsilon,R)=\mathbf{0}, \tag{20}$$

and $\mathbf{V}$ is the 3×3 potential matrix

$$\mathbf{V}(u,l,B,\Delta,I)=\begin{pmatrix}\Delta+V_e(u,l,B)-i\dfrac{\Gamma(u)}{2} & V_{eg}(u,l,B,I) & V_{pe}(u)\\ V_{eg}(u,l,B,I) & V_g(u,l) & 0\\ V_{pe}(u) & 0 & V_p(u,l,B)\end{pmatrix}. \tag{21}$$

The elements of $\mathbf{V}$ are described in Sec. II. A complex term $-i\Gamma(u)/2$ is added to the excited-state potential to simulate the effect of excited-state decay. The full retarded form of the molecular linewidth, Eq. (4), is used.

Application of standard asymptotic scattering boundary conditions to the three-component state vector $\boldsymbol{\phi}$ gives the *S*-matrix elements $S_{ij}(\varepsilon,l,B,\Delta,I)$. If $\varepsilon>\Delta$, all three channels are open: $i,j=g$, *p*, or *e*. When $\varepsilon<\Delta$, as is normally the case in our model, channel *e* is closed, and S_{ij} is only defined for $i,j=$ *g* or *p*. We choose the light intensity *I* low enough that the results are in the weak-field limit where the $P_{pg}=|S_{pg}|^2$ matrix element scales linearly in *I*. Our results are normalized to a standard intensity of $I=1$ mW/cm^2.

We find that we can make a change in the asymptotic shape of the artificial probe potential to make the model much more manageable computationally. The deep potential well of the excited state and the large kinetic energy in the probe channel require a small stepsize in u ($\lambdabar\Delta u\approx0.005a_0$). However, with the large range of $u[\lambdabar u_{\max}\approx(1500\text{–}3000)a_0]$ a small Δu increases the computation time and may compromise the numerical stability. Therefore, we modify the probe state potential to bring $V_p(u)$ to a small negative value at intermediate and asymptotic *u*. This results in a small asymptotic momentum $\hbar k$ in the probe channel, and allows us to gradually increase the stepsize to $\lambdabar\Delta u\approx0.5a_0$ as *u* increases. The coupling between the excited and probe states is turned off exponentially before the change in $V_p(u)$. The probabilities $|S_{pg}|^2$ and P_{pe} are completely independent of the asymptotic properties of the probe potential if there are no asymptotic barriers. Since we have no centrifugal potential in the asymptotic probe channel, there are no asymptotic centrifugal barriers. The presence of such barriers in our previously published model [20] resulted in some errors at larger l'' which we have now corrected in the present model.

The thermally averaged loss rate coefficient via state *e* is

$$K(\Delta,T)=\frac{k_BT}{hQ_T}\int_0^\infty\frac{d\varepsilon}{k_BT}e^{-\varepsilon/k_BT}\times\sum_{l''_{even},B}(2l''+1)|S_{pg}(\varepsilon,l'',B,\Delta,I)|^2, \tag{22}$$

where $Q_T=(2\pi\mu k_BT/h^2)^{3/2}$ is the translational partition function. Identical particle exchange symmetry ensures that only even partial waves exist for the ground state. We also define a nonaveraged rate coefficient for a fixed collision energy ε, where we define $T_\varepsilon \equiv \varepsilon/k_B$. Only the sum over partial waves and branches is performed:

$$K(\Delta,\varepsilon)=\frac{k_B T_\varepsilon}{hQ_{T_\varepsilon}}\sum_{l''_{even},B}(2l''+1)|S_{pg}(\varepsilon,l'',B,\Delta,I)|^2. \tag{23}$$

There are two possible cutoffs $l''_{\max}$ to the partial wave sum provided by the ground- and excited-state centrifugal potentials, respectively. For the ground state we can take $l''_{\max}$ to be the largest integer for which $\hbar^2 l''_{\max}(l''_{\max}+1)/2\mu R_C^2 < \varepsilon$ at the Condon point R_C. Thus, the Condon point is classically accessible for $l'' \leqslant l''_{\max}$ and classically forbidden for $l'' > l''_{\max}$. For the excited state, the centrifugal potential may create a barrier inside the Condon point for the $g \rightarrow e$ excitation. The position and the height of the barrier depend on J'. For collision energies around $\varepsilon = k_B T_D$ this barrier may prevent allowed ground-state partial waves from contributing to the loss, because the excited-state population never reaches the inner zone where RE decay and SC take place. In this case, $l''_{\max}$ may decrease from the value defined by the above inequality. We find that the ground-state cutoff applies except for the case of high energy and small detuning. In either case $|S_{pg}|^2$ decreases many orders of magnitude as l'' varies from $l''_{\max}$ over the next few l'' values. The upper limit for the sum in Eqs. (22) and (23) is set to the l''-value where $(2l''+1)|S_{pg}(\varepsilon,l'',B,\Delta,I)|^2$ is 10^{-6} of the maximum previous $(2l''+1)|S_{pg}(\varepsilon,l'',B,\Delta,I)|^2$ value.

B. Factorization of trap loss probability

The factorization in Eq. (1) allows us to separate the physics of the long-range excitation and the short-range decay to the trap loss channel. Reference [21] shows how to determine the short-range probability P_{pe} from a different coupled channels calculation where the complex decay term $-i\Gamma/2$ in Eq. (21) is omitted. Since P_{pe} is determined in a region near R_p where the local kinetic energy is very high in relation to ε, this probability is nearly independent of ε over a wide range. Therefore, we calculate [21]

$$P_{pe}(J')=|S_{pe}(\varepsilon>\Delta,l'',B=0,\Delta,I=0)|^2. \tag{24}$$

Here ε is taken above the threshold energy Δ where the e channel becomes open and S_{pe} is defined.

Our numerical calculations show, as expected, that P_{pe} is independent of ε over a wide range, typically of ε/k_B from 0.3 to 300 mK at low J' and 3 to 300 mK at high J', and also independent of Δ in our small range of detuning. The Landau-Zener interpretation of P_{pe} in Eq. (8) leads us to expect that P_{pe} will vary with J'. This variation should be stronger for the outer ${}^1\Pi_g$-${}^3\Sigma_g$ crossing than for the inner ${}^1\Sigma_u$-${}^3\Pi_u$ crossing. For the latter crossing, our calculations do give P_{pe} values which vary slowly with J'. We calculate $P_{pe}(J'=1)$ to be 0.024, 0.44, 0.31, 0.34, and 0.64 for Mg, Ca, Sr, Ba, and Yb, respectively. These probabilities are all large (order unity) except for the case of Mg. This qualitative conclusion is likely to be robust, even though our model calculations are only quite approximate.

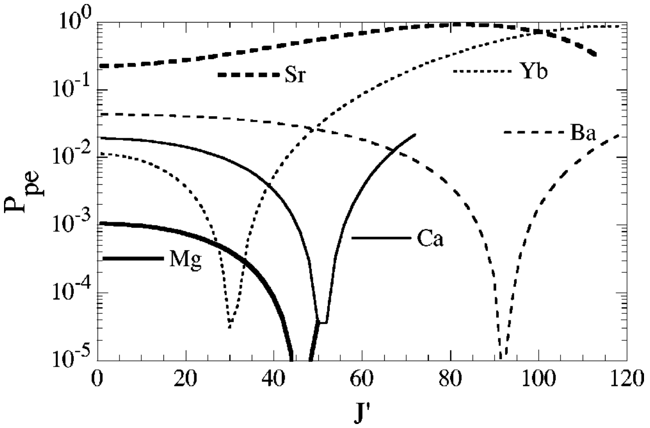

FIG. 4. Calculated probabilities $P_{pe}(J')$ versus J' for the ${}^1\Pi_g$-${}^3\Sigma_g$ SC crossing.

In contrast to our results for the ${}^1\Sigma_u$-${}^3\Pi_u$ crossing, Fig. 4 shows that the calculated $P_{pe}(J')$ values for the outer ${}^1\Pi_g$-${}^3\Sigma_g$ crossing indeed depend much more strongly on J'. A test of the Landau-Zener formula for Mg shows that the result of Eq. (8) is indistinguishable from the calculated line on the figure. The qualitative feature of a dip in P_{pe} as it goes near zero for some J' is associated with the phase factor in the LZ formula, Eq. (9). Since the specific J' range where this dip occurs is sensitive to the potentials used [37], our model calculations can only be a qualitative guide even for Mg. The relative values for the other species are also only qualitative guides, since other curve crossings are also involved. In any case, Sr is likely to have a large (order unity), perhaps the largest, P_{pe} for the ${}^1\Pi_g$ SC process.

We can use P_{pg} and P_{pe} from the close-coupling calculations to divide out the inner zone probability so as to define a numerical excitation-transfer function from the long-range region [21]

$$J_{eg}(\varepsilon,l'',B,\Delta,I)=\frac{P_{pg}(\varepsilon,l'',B,\Delta,I)}{P_{pe}(J')}, \tag{25}$$

where $J'=l''+B$. J_{eg} may be interpreted as the probability of reaching the short-range region due to optical excitation at long range and propagation to short range, including return after multiple vibrations across the short-range well. This interpretation follows from the fact that one gets the total trap loss probability $P_{pg}(\varepsilon,l'',B,\Delta,I)$ by multiplying $J_{eg}(\varepsilon,l'',B,\Delta,I)$ by the probability $P_{pe}(J')$ in Eq. (24) of a trap loss event in a single complete cycle across the well.

Using Eq. (25) we can define an excitation-transfer rate coefficient $\kappa(\Delta,\varepsilon)$

$$\kappa(\Delta,\varepsilon)=\frac{k_B T_\varepsilon}{hQ_{T_\varepsilon}}\sum_{l''_{even},B}(2l''+1)J_{ge}(\varepsilon,l'',B,\Delta,I). \tag{26}$$

This rate coefficient $\kappa(\Delta,\varepsilon)$ is related to the ordinary rate coefficient $K(\Delta,\varepsilon)$ in Eq. (23) through a mean inner zone probability $\langle P_{pe}(\varepsilon)\rangle$, which we can *define* by the relation

$$K(\Delta,\varepsilon)=\langle P_{pe}(\varepsilon)\rangle\kappa(\Delta,\varepsilon). \tag{27}$$

Clearly, we can also define a thermal average $\kappa(\Delta,T)$ analogous to that in Eq. (22), and define a thermal average $\langle P_{pe}(T)\rangle = K(\Delta,T)/\kappa(\Delta,T)$.

The usefulness of the factorization in Eq. (1) is that it allows us to define an excitation-transfer rate coefficient κ from which the inner zone SC probability has been removed [however, see the discussion in Sec. III C 3 about how a large $P_{pe}(J')$ may affect the width of resonance features]. We can predict much more confidently the properties of the long-range excitation and vibration than we can the short-range SC probabilities. Thus, once we have a better knowledge of these short-range probabilities, either through measurements or through better theoretical knowledge of potential curves and couplings, we can multiply our κ coefficients by $\langle P_{pe}(T)\rangle$ to get the SC rate coefficients.

C. Limiting cases of the excitation-transfer probability

The attractive molecular potentials support molecular vibrational levels with vibrational quantum numbers v, as described in Sec. II C. We can find simple analytic expressions for the excitation-transfer function $J_{eg}=J_{ee}P_{eg}$ factored according to Eq. (2) for two limiting cases: (1) strongly overlapping resonances where the probability is large for spontaneous decay during a single vibrational cycle, i.e., the level width is larger than the level spacing, and (2) nonoverlapping, or isolated, resonances, where many vibrations occur during a vibrational decay lifetime, i.e., the level width is much smaller than the level spacing. For group-II species, ${}^1\Sigma_u$ transitions at small detuning tend to be of the former type, but never become fully isolated in the detuning range we consider. On the other hand, ${}^1\Pi_g$ transitions tend to be of the latter type unless the detuning is very small or the SC probability is very large.

1. Small detuning and fast spontaneous decay

The quantum-mechanical theory of the first limiting case for trap loss for small detuning and fast radiative decay has been worked out in detail in Refs. [21,41,42,24], where

$$J_{eg}(\varepsilon,l'',B,\Delta,I)=J_{ee}(\varepsilon,l'',B,\Delta)P_{eg}(\varepsilon,l'',B,\Delta,I). \tag{28}$$

The factor

$$P_{eg}(\varepsilon,l'',B,\Delta,I)=1-e^{-2\pi\Lambda},$$

$$\Lambda=|V_{eg}(R_C)|^2/(\hbar v_C D_C), \tag{29}$$

where v_C and D_C are the speed and slope difference at the Condon point, represents the Landau-Zener probability of excitation from the ground state to the excited state in a one-way passage through the Condon point at R_C. In this limit, radiative decay is faster than the vibrational period ($\Gamma_v \gg h\nu_v$), there are no multiple vibrations, and the excited-state transfer factor

$$J_{ee}(\varepsilon,l'',B,\Delta)=e^{-a_{out}}\ll 1,$$

$$a_{out}=\lambdabar\int_{u_C}^{u_p} du\,\frac{\Gamma(u)}{\hbar v(u)} \tag{30}$$

represents the probability of survival along the classical trajectory from the Condon point of excitation to the point R_p of inner zone curve crossing; $v(u)=\{2[\varepsilon-V_e(u)-\Delta]/\mu\}^{1/2}$ is the local classical speed.

Note that the Landau-Zener expression for P_{eg} in Eq. (29) does not have the proper Wigner law threshold behavior, since J_{eg} should be proportional to k at low collision energy. However, our numerical J_{eg} will have the proper Wigner law form. Note also that the quantum-mechanical calculations in Refs. [21,24,41,42] support this semiclassical picture of localized excitation at the Condon point, not the delocalized excitation picture of the Gallagher-Pritchard (GP) model [43], which for small detuning predicts a dominant contribution to trap loss from off-resonant excitation at distances much less than R_C. The GP model also does not satisfy the Wigner law at low *T*. We defer detailed comparisons with semiclassical theories to a future publication.

2. Nonoverlapping resonances

The second limiting case is that of nonoverlapping vibrational resonances, that is, the spacing $h\nu_v$ [see Eq. (6)] between vibrational levels v is much larger than their total width Γ_v. This is typical of large detuning. Then $|S_{pg}|^2$ is given by an isolated Breit-Wigner resonance scattering formula for photoassociation lines [38,44]:

$$P_{pg}=\frac{\Gamma_{vp}\Gamma_{vg}}{[\varepsilon-(E_v+s_v)]^2+(\Gamma_v/2)^2}. \tag{31}$$

Here $E_v=\Delta-\varepsilon_v$ is the detuning-dependent position of the vibrational level in the molecule-field picture relative to the ground-state separated atom energy (when $\Delta=\varepsilon_v$, then $E_v=0$ and the vibrational level is in exact resonance with colliding atoms with zero kinetic energy), s_v is a level shift due to the laser-induced coupling, and the total width $\Gamma_v=\Gamma_{vp}+\Gamma_{vg}+\Gamma_{v,rad}$ is the sum of the decay widths into the probe (Γ_{vp}) and ground-state (Γ_{vg}) channels and the radiative decay rate ($\Gamma_{v,rad}$). In the weak decay limit ($\Gamma_v \ll h\nu_v$), we can write the Fermi golden rule decay widths as [45,46]

$$\Gamma_{vi}=2\pi|\langle v|V_{vi}|\varepsilon,l\rangle|^2=\hbar\nu_v P_{vi}, \tag{32}$$

where $i=g$ or p, l is the partial wave for channel *i*, and P_{vi} represents the probability of decay during a *single cycle* of vibration from level v to channel *i*. For the SC process, P_{vp} is a very weak function of energy as long as the detuning is not too large, and we can take $P_{vp}=P_{pe}$, where P_{pe} is the energy-independent SC probability discussed in Sec. III B. In the weak-field limit, Γ_{vg} is very small in relation to $\Gamma_{v,rad}$, and we can ignore it (that is, there is no power broadening).

Using Eq. (32) in Eq. (31), we get the factorization in Eq. (28) with the resonant-enhanced transfer function

$$J_{ee}=\frac{(\hbar\nu_v)^2}{[\varepsilon-(E_v+s_v)]^2+(\Gamma_v/2)^2}. \tag{33}$$

If we use the *reflection approximation* for the Franck-Condon factor in Γ_{vg} [34,35,44], then

$$P_{eg}=4\pi^2|V_{eg}(R_C)|^2\frac{1}{D_C}|\phi_g(\varepsilon,l'',R_C)|^2. \tag{34}$$

Equation (34) may be used throughout the whole cold collision domain (mK to nK). It satisfies the the correct Wigner threshold law behavior at low energies because of the $|\phi_g|^2$ factor. In the *s*-wave limit for low temperature, we may take the asymptotic form of the ground-state wave function and obtain

$$P_{eg}=16\pi^2\frac{|V_{eg}(R_C)|^2}{hv_\infty D_C}\sin^2 k(R_C-A_0). \tag{35}$$

This looks just like the Landau-Zener result in Eq. (8), except that the asymptotic speed v_∞ appears in the denominator instead of v_C [34], and the correct quantum phase appears in the sine factor instead of a semiclassical phase.

3. Contributions to the linewidths

The expression, Eq. (28), for J_{eg} in the limit of small detuning and fast decay does not depend in any way on the short-range SC probability. However, in the expression for J_{eg} in the isolated resonance limit, the width Γ_v in the J_{ee} factor, Eq. (33), does depend on P_{pe} through the contribution of $\Gamma_{vp}=\hbar\nu_v P_{pe}$. As long as Γ_{vp} is small compared to $\Gamma_{v,rad}$, the total width Γ_v is determined primarily by $\Gamma_{v,rad}$, and the shape of trap loss spectral lines will still be nearly independent of P_{pe}. However, if Γ_{vp} makes a significant contribution to the total width, the long-range excitation-transfer function J_{eg} will show additional broadening dependent on the magnitude of P_{pe}.

The total radiative decay width $\Gamma_{v,rad}$ can be calculated from the long-range form of the decay rates in Eqs. (4), using the excellent semiclassical approximation [47], $\langle v|\Gamma(u)|v\rangle=\nu_v\oint_v(\Gamma(u)/v(u))\bar{\lambda}\,du$, where the semiclassical integral is over a complete vibrational cycle. When $R_C<\bar{\lambda}$, we can use the lead term in the expansion of $\Gamma(u)$ in u in Eqs. (4), so that

$$\Gamma_{v,rad}(^1\Sigma_u)=2\Gamma_{\text{at}}=\text{const}, \tag{36}$$

$$\Gamma_{v,rad}(^1\Pi_g)=\Gamma_{\text{at}}\frac{\pi}{20a_3}u_C^2=0.701\Gamma_C(^1\Pi_g), \tag{37}$$

where a_3 is defined after Eq. (5) and $\Gamma_C(^1\Pi_g)$ is evaluated at the outer turning point of the vibration, which is almost the same as the Condon point.

For the detuning range we consider, the radiative width of $^1\Sigma_u$ levels, $2\Gamma_{\text{at}}$, is much larger than Γ_{vp}, which can be calculated from Eq. (32) using the probabilities listed in Sec. III B. Thus, $\Gamma_v\approx\Gamma_{v,rad}$ so that the *shape* of $^1\Sigma_u$ features (that is, their spacings and widths) should be well determined in our calculations.

Figure 5 shows $\Gamma_{v,rad}$ and Γ_{vp} for $^1\Pi_g$ features for Mg, Ca, and Sr. In our detuning range, $\Gamma_{v,rad}\gg\Gamma_{vp}$ for Mg. Thus, the shape of Mg $^1\Pi_g$ features should also be well determined in our calculations. On the other hand, for Ca and Sr, the Γ_{vp} is larger due to the larger P_{pe}. Γ_{vp} increases as $\Delta^{5/6}$ due to the ν_v factor in Eq. (32), and becomes larger than $\Gamma_{v,rad}$ near $\Delta=5\Gamma_{\text{at}}$ in our model for Sr and near $20\Gamma_{\text{at}}$ for Ca. Thus, we can expect predissociation broadening of $^1\Pi_g$ features to become observable for Ca or Sr at relatively small detunings. Measurements of such widths could lead to experimental information about P_{pe} for the $^1\Pi_g$ state. On the other hand, our calculated model line shapes should only be viewed as a qualitative guide in a region where $\Gamma_{vp}\gg\Gamma_{v,rad}$.

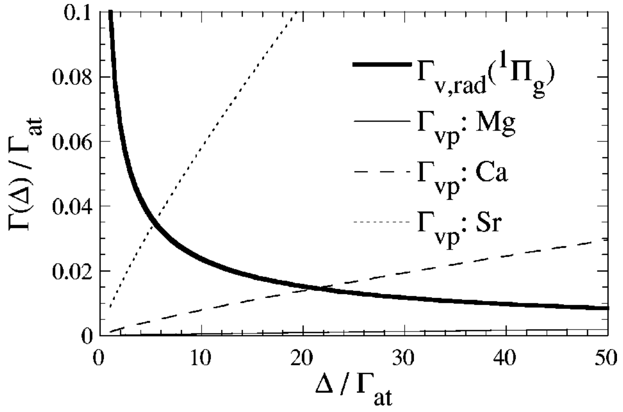

FIG. 5. Radiative width $\Gamma_{v,rad}$ for Mg and widths Γ_{vp} for Mg, Ca and Sr versus Δ for the $^1\Pi_g$-$^3\Sigma_g$ SC crossing.

D. Radiative escape calculations

The calculation of the RE trap loss rate coefficient follows the factorization procedure in Eq. (1) as for the SC process. The RE loss is not due to a single curve crossing, but rather to excited state emission from the distance range $R<R_p=\bar{\lambda}u_p$, where u_p is the point for which a kinetic-energy increase of 1 K for the atom pair has been gained after excitation (the 1 K is arbitrary—we only choose it to represent a “standard” loss energy). Clearly, RE can only be significant for the $^1\Sigma_u$ state because of the negligible short-range emission from the $^1\Pi_g$ state. We calculate the total probability of radiative escape, $P_{pe}=P_{\text{decay}}$ during a complete cycle of vibration across the region $u<u_p$ by integrating along the classical trajectory

$$P_{\text{decay}}(\varepsilon,J',\Delta)=1-\exp(-a),$$

$$a=2\bar{\lambda}\int_{u_p}^{u_{in}}du\,\frac{\Gamma(u)}{\hbar v(u)}. \tag{38}$$

P_{decay} depends only weakly on Δ, J'. Variations with ε at the highest collision energies also play a role when calculating the thermally averaged rate. The main contribution to P_{decay} comes from the long-range region where the potential is determined by its analytic long-range form.

The P_{decay} probability is insensitive to collision energy and detuning. In the detuning range $\Delta/\Gamma_{\text{at}}$ from 1 to 50 and for a collision energy of k_BT_D, we find that P_{decay} ranges from 0.157 to 0.144 for Mg, 0.103 to 0.100 for Ca, 0.147 to

0.142 for Sr, 0.113 to 0.110 for Ba, and 0.149 to 0.145 for Yb. These hardly change at all at a collision energy of $k_BT_D/1000$, for example, changing to 0.105 to 0.100 for Ca.

We have also used a calculation with an artificial probe state crossing the excited-state potential at R_p ($R_p \approx 150a_0$ for our Mg model for $J'=1$), as described in Sec. II G, to calculate the excitation-transfer function J_{eg} appropriate to the RE process. We find, as expected, that the numerical J_{eg} function calculated this way is very nearly the same as the one calculated using the SC R_p at much shorter range. For our detuning range the radiative contribution to the total width Γ_v of $^1\Sigma_u$ levels is much larger than contribution due to predissociation to the SC channel.

We expect that our radiative escape trap loss calculations are reliable in magnitude, since only long-range properties are relevant in determining both J_{eg} and P_{decay}. Therefore, in the next section we can confidently give absolute magnitudes for the RE contribution to the total trap loss rate coefficient $K(\Delta,T)$ for all alkaline-earth-metal atoms we study here.

IV. RESULTS

A. Trap loss for Mg at $T=T_D$

Our calculated results for $T_D=1.9$ mK for Mg collisions are shown in Figs. 6(a), 7(a), and 8(a). These results are different from the results presented in Ref. [20], since we have corrected some errors we made in the sum over partial waves in that reference [48]. Figure 6(a) shows on a logarithmic scale the separate contributions of each SC or RE process to the thermally averaged rate constant $K(\Delta,T)$ from Eq. (22), whereas Fig. 7(a) shows the corresponding results for $K(\Delta,\varepsilon)$ at a single collision energy ε. Figure 8(a) shows on a linear scale the sum of contributions from all loss processes, and shows what one might expect to see in a laboratory spectrum.

The dominant loss process for Mg at 1.9 mK is due to RE from the $^1\Sigma_u$ state. The spectra for $^1\Sigma_u$ RE and SC processes have the same shape, since they have the same excitation-transfer function κ. The RE and SC processes differ only by a multiplicative factor that is nearly independent of Δ, due to the different P_{pe} factors for RE and SC. The $^1\Sigma_u$ RE probability only varies by 0.157 to 0.144 from detunings of 1 to 50 Γ_{at}, whereas the $^1\Sigma_u$ SC probability is constant over this range. The $^1\Sigma_u$ spectra in Figs. 6(a) and 7(a) are nearly the same, since the broad features do not change much upon thermal averaging. The rate coefficient becomes very small as detuning decreases below 2 or 3 Γ_{at}. This is because $J_{ee} \ll 1$ for very small detuning due to spontaneous-emission during the long-range approach of the two atoms. Spontaneous-emission losses become small for detunings larger than around $10\Gamma_{\text{at}}$, and vibrationally resolved, but rotationally unresolved, photoassociation structure begins to develop as detuning increases. This occurs as the spacing between adjacent $^1\Sigma_u$ vibrational levels from Eq. (6) becomes larger than the radiative decay width. Several rotational features with different J' may contribute to each of the broad photoassociation resonances, with the range of J' depending on detuning. Each individual $^1\Sigma_u$ rotational line has a width on the order of $(2\Gamma_{\text{at}}+k_BT)/h \approx$ 200 MHz. There is negligible predissociation broadening due to SC processes in this region of the spectrum.

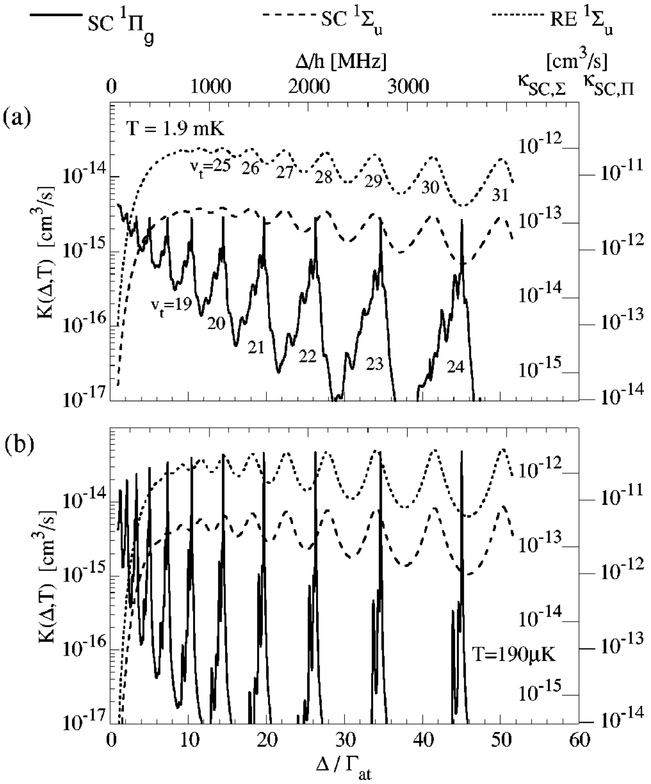

FIG. 6. Contributions from the $^1\Sigma_u$ RE and $^1\Sigma_u$ and $^1\Pi_g$ SC processes to the thermally averaged loss rate coefficient $K(\Delta,T)$ at (a) 1.9 mK and (b) 190 μK as a function of laser detuning Δ for Mg at a standard laser intensity $I=1$ mW/cm^2. The scales for the excitation-transfer coefficients, $\kappa(\Delta,T)$, for the SC processes are indicated by the vertical axes to the right. The vibrational quantum numbers from the top of the potential v_t are indicated for $^1\Sigma_u$ and $^1\Pi_g$ features.

Using Eq. (5) in Sec. II C, the vibrational quantum number v_t, as counted down from the top of the potential at the dissociation limit, can be given for the resolved, or partially resolved, features in the trap loss spectrum. We define v_t to be $v_D - v$ rounded up to the next integer. Each integer v_t value defines an energy range that contains only one vibrational level for a given J. The v_t quantum numbers for $^1\Sigma_u$ and $^1\Pi_g$ features are indicated on Fig. 7. Note that there are many levels (not calculated) within the range $\Delta/\Gamma_{\text{at}}<1$, a range where Eq. (5) is not meaningful due to retardation effects on the potential. The broad $^1\Sigma_u$ features provide an example of overlapping resonances, analogous to those treated by Bell and Seaton [49], for the case of dielectronic recombination where the spacing between collisional resonance levels becomes less than their radiative decay width.

The contribution to $K(\Delta,T)$ from the $^1\Pi_g$ SC process shows much sharper vibrational structure than the corresponding $^1\Sigma_u$ spectrum. This is because of the small radiative widths of the $^1\Pi_g$ levels, which become even smaller as Δ increases. The individual contribution from a number of narrow rotational levels is evident in Fig. 7(a). Figure 6(a)

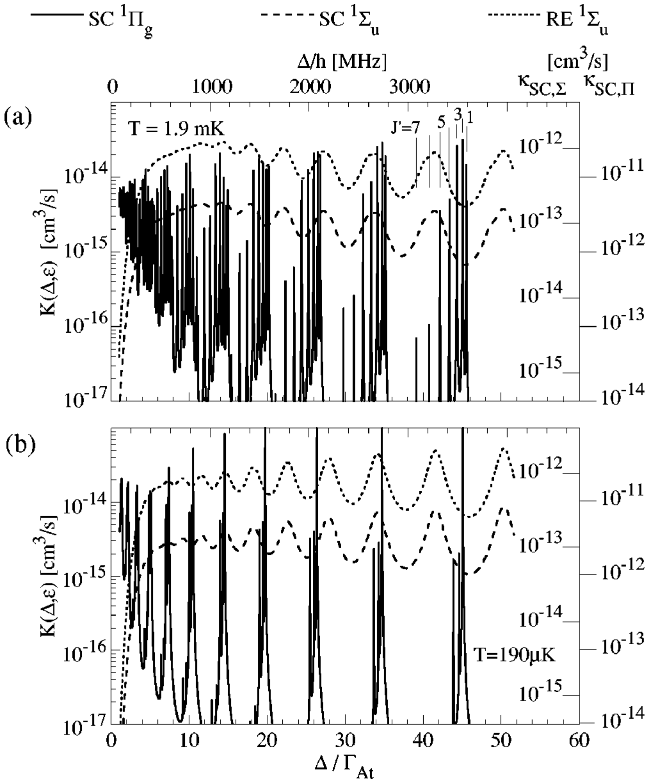

FIG. 7. Contributions from the $^1\Sigma_u$ RE and $^1\Sigma_u$ and $^1\Pi_g$ SC processes to the loss rate coefficients $K(\Delta,\varepsilon)$ at a fixed collision energy (a) $\varepsilon = k_B$ (1.9 mK) (b) $\varepsilon = k_B$ (190 μK) as a function of laser detuning Δ for Mg at laser intensity $I = 1$ mW/cm^2. $K(\Delta,\varepsilon)$ is a sum over partial waves and branches for $\varepsilon = k_B T$. The corresponding excitation-transfer coefficients $\kappa(\Delta,\varepsilon)$ are indicated by the vertical axis to the right. Excited-state rotational quantum numbers are indicated for the $v_t = 24$ $^1\Pi_g$ feature in (a).

shows that this $^1\Pi_g$ structure even survives thermal averaging. Figure 8(a) shows that sharp $^1\Pi_g$ features can even survive thermal averaging at 1.9 mK, although such features are quite weak for Mg and would be hard to see (however, see below for Ca and Ba, where such features might be observable). We find that there are sharp $J' = 1$ $^1\Pi_g$ features due to *s*-wave collisions that can be much narrower than $k_B T$ (which is about 40 MHz at 1.9 mK), whereas features due to $l'' > 0$ collisions have widths on the order of $k_B T$. This *s*-wave behavior is evident in our numerical calculations, but can be easily explained in terms of the analytic behavior of the isolated line shapes using Eqs. (31), (32), and (34). We will discuss this *s*-wave resonance narrowing feature elsewhere [51].

Figures 6 and 8 both show that at very small detuning, on the order of 1 or 2 Γ_{at}, the trap loss is dominated by SC due to the $^1\Pi_g$ state. The increasing radiative transition probability as detuning decreases, and the near absence of spontaneous emission losses for the weakly emitting state, ensures that the $^1\Pi_g$ contribution to trap loss must be dominant at very small Δ. We will show in the next section that this is even more important for the heavier species. Our conclusion concerning the role of the $^1\Pi_g$ state at small Δ agrees with the findings of Refs. [7,20].

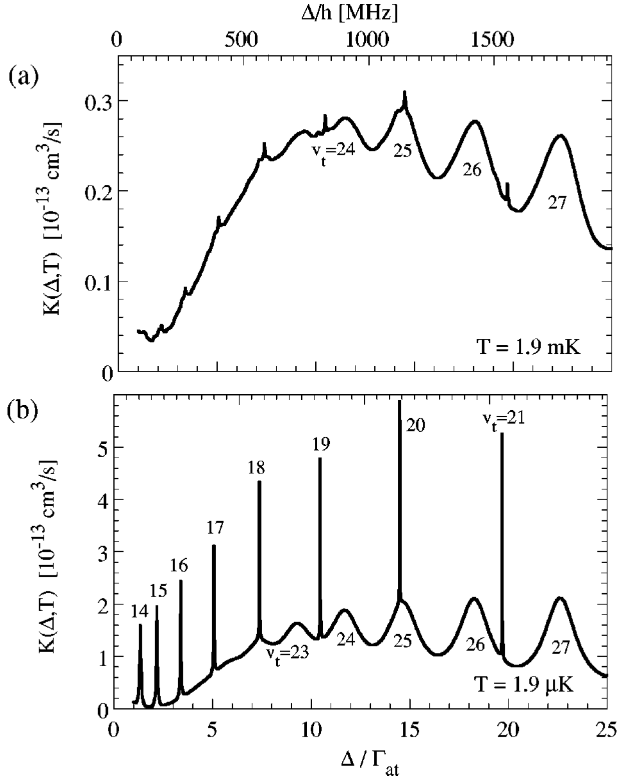

FIG. 8. Total thermally averaged Mg spectrum $K(\Delta,T)$ summed over all RE and SC contributions on a linear scale (a) at $T_D = 1.9$ mK, and (b) in the *s*-wave limit at $T = 1.9$ μK. The vibrational quantum numbers v_t are indicated for the $^1\Sigma_u$ and $^1\Pi_g$ features. Only excited $J' = 1$ levels contribute *R*-branch transition from *s* waves in panel (b).

Figures 6(b) and 7(b) show the contributions to SC and RE processes for Mg at 190 μK. The broad $^1\Sigma_u$ features are not very sensitive to changing the temperature. They narrow slightly at the lower temperature. However, the $^1\Pi_g$ features simplify and clearly have contributions from fewer partial waves. The effect of thermal averaging on $^1\Pi_g$ features is to cause some broadening, with a consequent decrease in peak height.

B. Trap loss for Mg near 1 μK

Figure 8(b) shows $K(\Delta,T)$ summed over all components at the extremely cold temperature of 1.9 μK. This is deeply in the Wigner law domain, where only *s*-wave collisions contribute to the spectrum, and the rate constant $K(\Delta,T)$ becomes independent of T [1]. The broad $^1\Sigma_u$ features are similar to the ones at higher temperature, but are due only to absorption by a single R branch line from $l'' = 0$ to a $J' = 1$ $^1\Sigma_u$ level. The only significant broadening is due to radiative decay. On the other hand, the $^1\Pi_g$ features, also due to a single R branch line from $l'' = 0$ to a $J' = 1$ $^1\Pi_g$ level, become prominent sharp features in the spectrum, having widths on the order of a few MHz due to radiative decay. Even the level near $1\Gamma_{\text{at}}$ detuning is quite sharp and isolated. Section II E discusses why we expect to get the vibrational spacings right, although we do not expect to predict correctly

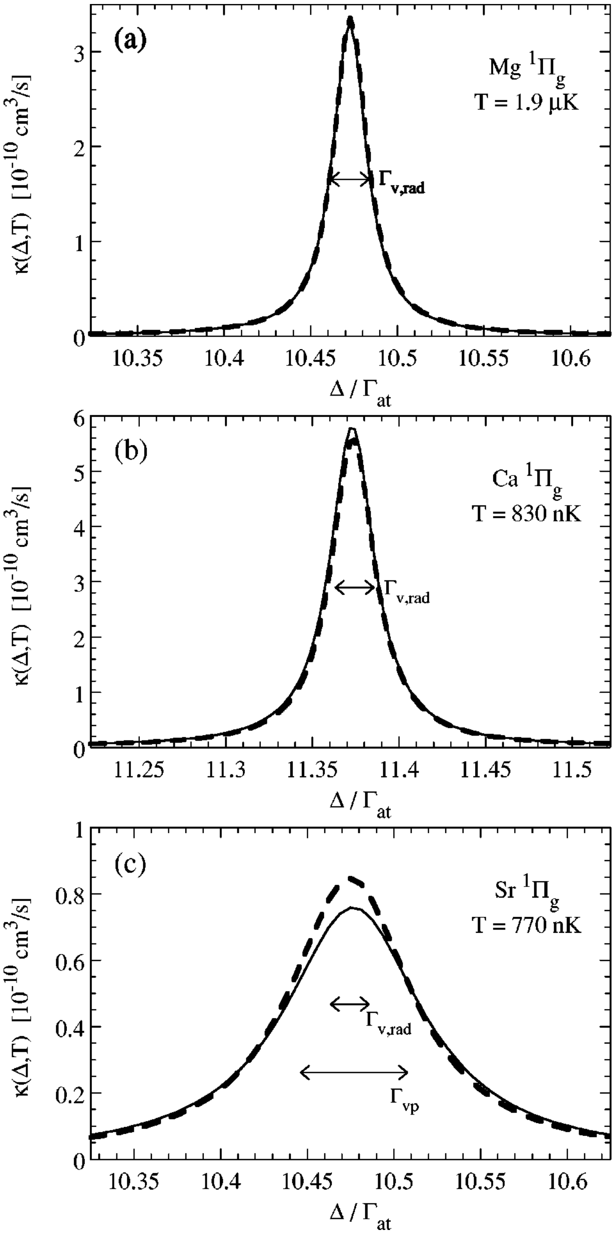

FIG. 9. Single $^1\Pi_g$ vibrational feature in the vicinity of $\Delta \approx 10\Gamma_{\text{at}}$ for (a) Mg, (b) Ca, and (c) Sr. The figure shows the quality of the isolated resonance approximation for the excitation-transfer line shape $\kappa(\Delta,T)$. The solid line is the complex potential numerical calculation, and the dashed line is the analytic line shape based on Eqs. (28), (33), and (35).

the actual position of levels, which depend on an unknown phase due to the short-range $^1\Pi_g$ potential.

Figure 9(a) shows the excellent quality of the isolated resonance approximation for a Mg $^1\Pi_g$ s-wave absorption feature due to a single vibrational level. This approximation should be good in this case, since the mean vibrational spacing near this level is 280 MHz, which is much larger than the width. The figure compares the numerical line shape with that calculated using the isolated resonance formulas discussed in Sec. III C. The analytic formula calculates the factors in Eqs. (28), which are used in Eq. (26), by making the isolated resonance approximation, Eq. (33), and the reflection approximation, Eq. (35). The linewidth in the denominator of Eq. (33), calculated to be 1.6 MHz from Eq. (37), is almost entirely due to weak spontaneous decay of this $^1\Pi_g$ level, as discussed Sec. III C in relation to Fig. 5. Any broadening due to thermal averaging is negligible, since $k_BT/h = 0.04$ MHz.

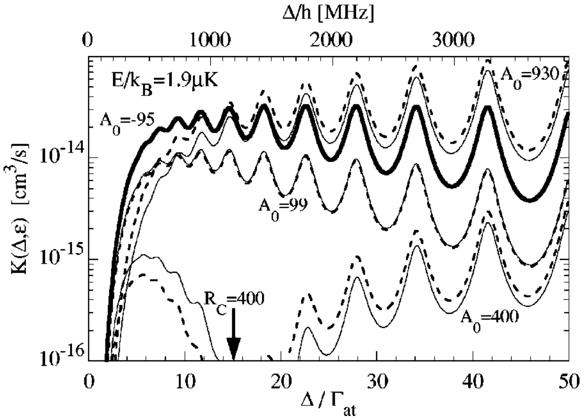

FIG. 10. Scaling with different scattering lengths of $K(\Delta,\varepsilon)$ for the $^1\Sigma_u$ transition in Mg. The bold solid line shows the numerically calculated $K(\Delta,\varepsilon)$ at $\varepsilon = k_B(1.9\ \mu\text{K})$ for the "standard" ground-state model potential with $A_0 = -95a_0$. The other solid lines show the calculated $K(\Delta,\varepsilon)$ for three other model potentials with different scattering lengths of $99a_0$, $400a_0$, and $930a_0$. The dashed line shows the scaled $K(\Delta,\varepsilon)$ calculated from the standard one using the scaling based on Eq. (35), as discussed in the text. The detuning for which the Condon point is $400a_0$ is indicated by the arrow. The effect of the node in the ground-state wave function is evident for the $A_0 = 400a_0$ case.

We have verified that our thermal spectrum at relatively high temperature, 1.9 mK, is to a good approximation independent of the choice of the ground-state potential, as discussed in Sec. II D. This is because of the need to sum over several partial waves, for which the phase of the ground-state wave function varies by more than π. In addition, the need to average over a range of collision energies also contributes a range of phase variation to the ground-state wave function.

The spectrum at very low temperature, on the other hand, is sensitive to the phase of the ground-state wave function, which is generally unknown for group-II species and strongly dependent of the details of the ground-state potential. This sensitivity is explained by the reflection approximation in Eq. (35), which shows P_{eg} is proportional to $\sin^2 k(R_C - A_0)$. We have just seen that the reflection approximation is excellent for isolated resonance line shapes. Therefore, if we know $K(\Delta,T)$ in the s-wave domain for one scattering length A_0, and if we have a different potential with a different scattering length A_0', the $K(\Delta,T)$ for the new case can be scaled from the original one by multiplying by the ratio $\sin^2 k(R_C - A_0')/\sin^2 k(R_C - A_0)$. Figure 10 compares this scaling (dashed lines) to numerical calculations (solid lines) for several different model ground-state potentials with different A_0'. The former are scaled from our original calculation, for which $A_0 = -95\ a_0$. Figure 10 demonstrates that this scaling is a good approximation, even when the scatter-

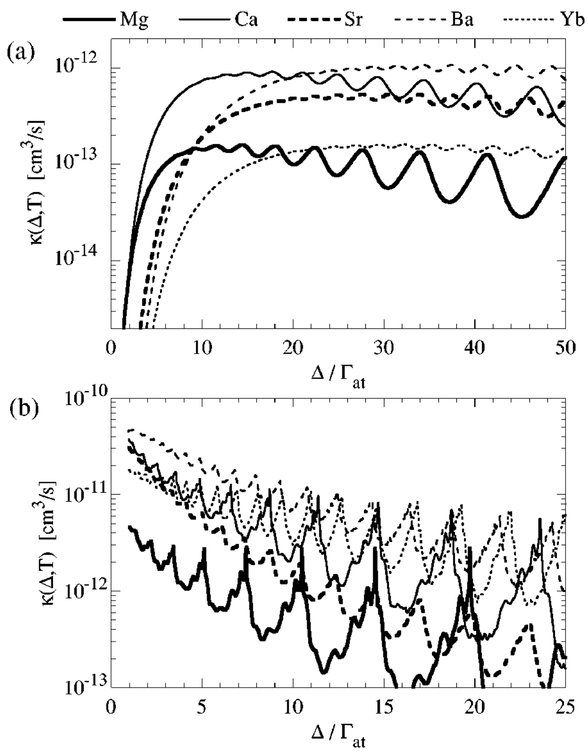

FIG. 11. Excitation transfer coefficients $\kappa(\Delta,\varepsilon)$ on a logarithmic scale for the (a) $^1\Sigma_u$ and (b) $^1\Pi_g$ states as a function of laser detuning Δ for Mg, Ca, Sr, Ba, and Yb at a laser intensity of $I = 1$ mW/cm^2.

ing length is unusually large and even for overlapping $^1\Sigma_u$ features. The scaling relation is excellent at small Δ for scattering lengths having magnitudes up to a few times x_0 (defined in Sec. II D and having a value of $36a_0$ for Mg). The scaling is even a reasonable approximation for the case where $A_0' = 400a_0$ and the ground-state wave function has a node at $R_C = A_0'$ near $\Delta/\Gamma_{\rm at} = 15$. The node for the $A_0' = 930a_0$ case occurs for $\Delta/\Gamma_{\rm at} < 1$ and is off scale in Fig. 10 for the $A_0' = 99a_0$ case.

V. OTHER ALKALINE EARTH-METAL ATOMS

Our calculations for the other group-II species and Yb are shown in Figs. 9(b), 9(c), 11, 12, and 13. We trust that these model calculations, which can only provide order of magnitude estimates for SC probabilities and predissociation contributions to linewidths, will provide a useful qualitative guide to differences and similarities among the various cases to guide future experiments on these systems. Our calculations should be fairly robust with respect to qualitative expectations as to the different kinds of features to expect in trap loss spectra.

Figure 9(b) shows that a very low temperature Ca $^1\Pi_g$ feature is very similar to the Mg one previously discussed. The total width is slightly larger than the radiative width due to weak predissociation of this feature (see Fig. 5). The effect of the large predissociation width, where $\Gamma_{vp} > \Gamma_{\rm rad}$, is evident for the Sr feature in Fig. 9(c). The isolated resonance approximation is also beginning to fail for Sr lines because

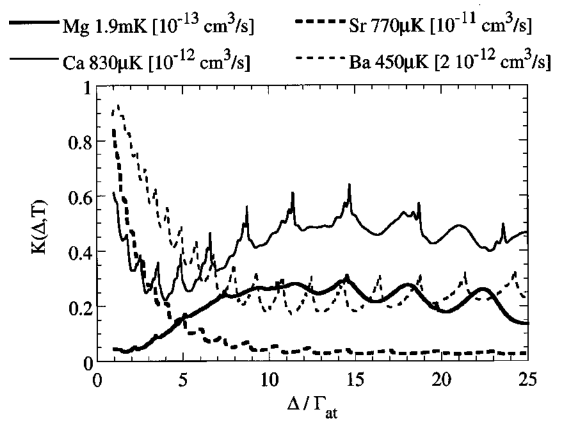

FIG. 12. Spectrum $K(\Delta,T)$ summed over all RE and SC contributions at T_D for Mg, Ca, Sr, and Ba at a laser intensity of $I = 1$ mW/cm^2.

of the strong predissociation broadening in our model with $P_{pe} = 0.22$ (see Fig. 4). Although our model calculation for Sr predissociation widths should not be considered to be reliable, the model does show that if the widths of $^1\Pi_g$ features like the one in Fig. 9(c) could be measured, the data should allow a value to be determined for P_{pe}. Since temperatures in the nK regime have already been reported for intercombination line cooling of Sr, it may be quite feasible to measure such widths.

Figure 11 shows the thermally averaged excitation-transfer coefficients $\kappa(\Delta,T)$ [see Eq. (26) and following] for the $^1\Sigma_u$ and $^1\Pi_g$ states in these systems at T_D for the ^1S

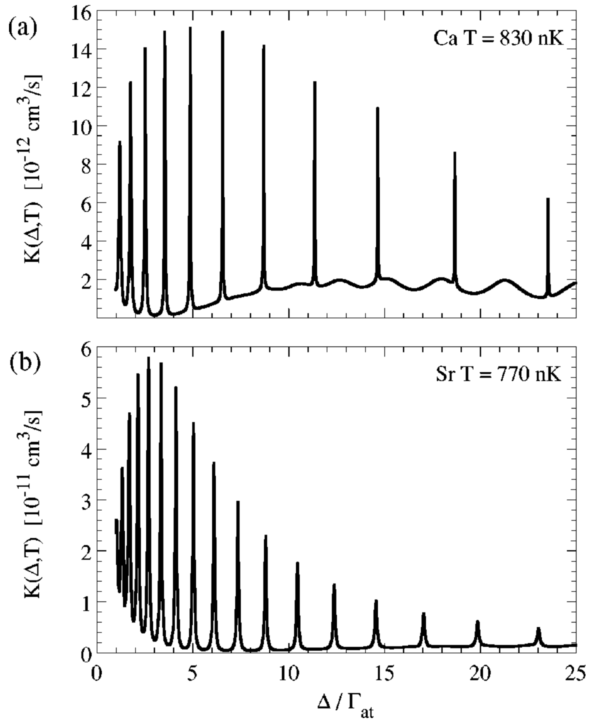

FIG. 13. Spectrum $K(\Delta,T)$ summed over all RE and SC contributions at the s-wave domain at $T_D/1000$ for (a) Ca and (b) Sr at a laser intensity of $I = 1$ mW/cm^2.

$\rightarrow {}^1P$ cooling transition. In spite of the fact that the inner zone SC probability P_{pe} is divided out of the expression for $\kappa(\Delta,T)$, there are still a number of differences among the different species. The differences in spacing and contrast of the individual vibrational features that appear at larger detuning is clearly related to the vibrational spacing, Eq. (6), which decreases with increasing mass. The differences in magnitude can be qualitatively related to the scaling of the different factors that make up $\kappa(\Delta,\varepsilon)$ in Eq. (26). There are four factors that contribute to the scaling: (1) $1/Q_T \rightarrow \mu^{-3/2}$, (2) the sum over $l'' \rightarrow l_{\max}^2 \rightarrow \mu d_0^{4/3}/\Delta^{2/3}$, (3) $J_{ee}(\text{peak}) \rightarrow (\nu_v/\Gamma_v)^2 \rightarrow \bar{\lambda}^6 \Delta^{5/3}/(\mu d_0^{16/3})$, and (4) $P_{eg} \rightarrow |V_{eg}(R_C)|^2/(vD_C) \rightarrow \mu^{1/2} d_0^{8/3}/\Delta^{4/3}$. The net scaling of the peak magnitude of $\kappa(\Delta,T)$ thus scales approximately as $\bar{\lambda}^6/(\mu d_0^{4/3}\Delta^{1/3})$. This gives scaling factors at the same Δ of 1, 5.0, 3.4, 6.4, 1.1 for Mg, Ca, Sr, Ba, and Yb, respectively (these factors should be scaled by an additional factor of $\bar{\lambda}/d_0^{2/3}$ if evaluated at the same scaled detuning, Δ/Γ_{at}). These scaling factors account for the relative magnitudes of the peak $\kappa(\Delta,T)$ for the ${}^1\Sigma_u$ state in Fig. 11(a) in the relatively flat region from 20 to 50 $\Delta/\Gamma_{\text{at}}$. The scaling for the ${}^1\Pi_g$ spectra in Fig. 11(b) also needs to take into account the predissociation contribution to the width Γ_v, which was taken to be purely radiative for the scaling of the ${}^1\Sigma_u$ spectrum in Fig. 11(a). For example, this extra predissociation broadening lowers the peak of Sr features below those for Mg in Fig. 11(b).

Figure 12 shows our model thermally averaged $K(\Delta,T)$ summed over all contributions. With the *caveat* that the relative contributions of SC processes are not likely to be reliable in our model calculations, these model spectra show qualitative features that one might observe in laboratory spectra. In particular, ${}^1\Pi_g$ SC processes make a dominant contribution to the small detuning trap loss for $\Delta <$ a few Γ_{at}. This has already been discussed in Refs. [7,20]. We can compare our results to the measured $2K(\Delta,T) = 4.5(0.3)(1.1)\times 10^{-10}$ cm^3/s [50] for Sr at $\Delta/\Gamma_{\text{at}} = 1.75$, $I = 60$ mW/cm^2, and $T \approx 4T_D$ [7]. Although the effect of a strong laser field needs to be investigated for this case, Ref. [24] suggests that near-linear scaling may apply to small detuning trap loss even in the strong field domain (see Fig. 6 of that reference). If we assume linear scaling with I, our calculated value for $T = T_D$ at $I = 1$ mW/cm^2 scales to a value of $2K = 6\times 10^{-10}$ cm^3/s at $I = 60$ mW/cm^2. The agreement of our very approximate model to within a factor of 2 with the measured result for Sr is gratifying and lends confidence to the usefulness of our estimates.

At present, there are no other data on Sr or other group-II species to which we can compare our calculations directly. The Ca_2 photoassociation spectra in a 3 mK Ca MOT reported by Zinner *et al.* in Ref. [17] extend over a detuning range from about 50 to 2700 Γ_{at}, which is larger than we calculate. They observed ${}^1\Sigma_u$ features and gave a detailed analysis of partially resolved rotational substructure for a feature near $\Delta = 27$ GHz $= 780\Gamma_{\text{at}}$. The fact that the width of this feature could be explained by a combination of natural and thermal broadening of several rotational lines implies that predissociation broadening makes a small contribution to the linewidth of this feature. If we assume that 20 MHz or less of the observed 150 MHz feature width is due to predissociation, we would then estimate the ${}^1\Sigma_u$ SC $P_{pe} < 0.05$, which is much less than the value 0.4 estimated by our model for Ca. Although our model should not be extrapolated to such large detuning without careful testing, this apparent inconsistency points out that much more detailed knowledge of potentials and matrix elements is needed for accurate calculations. It is an interesting fact to be explained why the apparent predissociation rate of ${}^1\Sigma_u$ levels in Ca_2 is relatively small, given the likelihood of several curve crossings with moderately large matrix elements (see Fig. 2).

Our calculations in Fig. 12 suggest that resolved structure due to ${}^1\Pi_g$ features may be seen at small detunings below around $25\Gamma_{\text{at}}$ for Ca and Ba. Structure for Sr is predicted to be suppressed by strong predissociation broadening. No ${}^1\Pi_g$ structure was reported for detunings larger than around $50\Gamma_{\text{at}}$ in Ref. [17]. Such ${}^1\Pi_g$ structure in Ca_2 at these larger detunings may be hard to see due to masking by the strong ${}^1\Sigma_u$ features.

Figure 13 shows our predictions for Ca and Sr features at extremely low $T = T_D/1000$. This is in the *s*-wave limit where the ${}^1\Pi_g$ structure becomes quite sharp, as discussed in relation to Fig. 9 above. In this domain sharp ${}^1\Pi_g$ features should be the dominant features in the trap loss spectrum. It is noteworthy that this structure is predicted to persist even to very small detunings on the order of Γ_{at}. Thus, if the Sr trap loss experiments of Ref. [7] could be repeated at these low temperatures, such features might be measurable. Figure 5 predicts that predissociation widths may be large enough for Sr_2 ${}^1\Pi_g$ features at even a few Γ_{at} detuning that observed broadening in the spectra might be able to determine P_{pe} for the Sr ${}^1\Pi_g$ SC process. Thus, low-temperature measurements provide for tests of consistency with high-temperature measurements.

VI. CONCLUSIONS

We have carried out model calculations of the small-detuning collisional trap loss spectrum of laser-cooled group-II species Mg, Ca, Sr, Ba, and also Yb. We consider detunings Δ up to 50 atomic linewidths Γ_{at} to the red of the ${}^1S_0 \rightarrow {}^1P_1$ laser-cooling transition for these species and treat both inelastic state-changing collisions and radiative loss. Although our calculations are only model calculations because the short-range molecular potentials are not known to sufficient accuracy, we do incorporate the correct long-range aspects of the potentials and spectra. These calculations are intended as a guide for developing experimental studies on these systems, which have the advantage that the collisions are not complicated by molecular hyperfine structure.

We consider both the mK range for Doppler cooling on the allowed ${}^1S_0 \rightarrow {}^1P_1$ transition, and the μK range for Doppler cooling on the ${}^1S_0 \rightarrow {}^3P_1$ intercombination transition. Collisions in the mK range involve many partial waves, whereas μK collisions only involve *s*-wave collisions. Our quantum-mechanical calculations avoid semiclassical approximations and properly account for the threshold properties of the collisions. Our interpretation of trap loss collision dynamics is based on a factorization of the overall probability into parts that represent long-range excitation, propagation to the short-range region, and short-range radiative or curve crossing processes that lead to loss. Thus, we can define an excitation-transfer coefficient $\kappa(\Delta,T)$, which, unlike the conventional rate coefficient $K(\Delta,T)$, offers a significant degree of independence from the details of unknown short-range processes. Our analysis shows how analytic formulas in the limits of small or large detuning can be used to interpret the trap loss spectrum. These formulas show how the low-temperature photoassociation spectrum is expected to scale for different values of the unknown *s*-wave scattering length.

The trap loss spectra in all the group-II systems are influenced by two molecular transitions, the dipole-allowed ${}^1\Sigma_g \rightarrow {}^1\Sigma_u$ transtion and the dipole-forbidden ${}^1\Sigma_g \rightarrow {}^1\Pi_g$ transition. The latter becomes allowed at long range because of retardation corrections to the transition-matrix element. The ${}^1\Sigma_u$ features are structureless at small detuning and reduced in magnitude due to spontaneous decay of the excited state as the atoms approach one another on the excited-state molecular potential. They show broad vibrationally resolved but rotationally unresolved photoassociation structure as detuning increases away from atomic resonance. On the other hand, the ${}^1\Pi_g$ absorption always dominates at small detuning. Resolved ${}^1\Pi_g$ vibrational and rotational photoassociation structure can persist even to small detuning, and should be especially prominent at very low temperature. Measurement of the widths of such features could lead to information about the short-range probability of the state-changing collisions, at least for the heavier group-II elements.

There are only very limited data with which we can compare our calculations. Our model calculations agree within a factor of 2 with the measured Sr trap loss rate coefficient at a single detuning. Photoassociation spectra for Ca only exist for much larger detuning than we consider here, but suggest that the probability of the ${}^1\Sigma_u$ state changing process may be much smaller than our model calculations indicate. The time is right for more detailed and complete experimental studies on these group-II systems. Recent experimental advances in group-II cooling and trapping suggest that such studies will be forthcoming. A number of other directions are also open for continuing experimental and theoretical studies, for example, trap loss collisions near the ${}^1S_0 \rightarrow {}^3P_1$ intercombination line, or collisions associated with two ${}^1P_1$ atoms or two ${}^3P$ atoms.

ACKNOWLEDGMENTS

This work was supported by the Academy of Finland (Project Nos. 43336 and No. 50314), the European Union Cold Atoms and Ultraprecise Atomic Clocks Network, Nordita, NorFA, the Carlsberg Foundation, and the U.S. Office of Naval Research. We thank Nils Andersen, Alan Gallagher, Ernst Rasel, Klaus Sengstock, Jan Thomsen, and Carl Williams for discussions, and E. Czuchaj for sending us the new Mg_2 results.

---

[1] J. Weiner, V. Bagnato, S. Zilio, and P. S. Julienne, Rev. Mod. Phys. **71**, 1 (1999).

[2] D. Sesko, T. Walker, C. Monroe, A. Gallagher, and C. Wieman, Phys. Rev. Lett. **63**, 961 (1989).

[3] Noble-gas atoms are another group of atoms that have been extensively laser cooled. The number of collision channels for these atoms is less than for alkali-metal atoms, but the collisional loss processes are dominated by Penning ionization.

[4] K. M. Jones, P. S. Julienne, P. D. Lett, W. D. Phillips, E. Tiesinga, and C. J. Williams, Europhys. Lett. **35**, 85 (1996).

[5] J. P. Burke, Jr., C. H. Greene, J. L. Bohn, H. Wang, P. L. Gould, and W. C. Stwalley, Phys. Rev. A **60**, 4417 (1999).

[6] C. J. Williams, E. Tiesinga, P. S. Julienne, H. Wang, W. C. Stwalley, and P. L. Gould, Phys. Rev. A **60**, 4427 (1999).

[7] T. P. Dinneen, K. R. Vogel, E. Arimondo, J. L. Hall, and A. Gallagher, Phys. Rev. A **59**, 1216 (1999).

[8] H. Katori, T. Ido, Y. Isoya, and M. Kuwata-Gonokami, Phys. Rev. Lett. **82**, 1116 (1999).

[9] H. Katori, T. Ido, and M. Kuwata-Gonokami, J. Phys. Soc. Jpn. **68**, 2479 (1999).

[10] T. Ido, Y. Isoya, and H. Katori, Phys. Rev. A **61**, 061403 (2000).

[11] H. Katori, T. Ido, Y. Isoya, and M. Kuwata-Gonokami (unpublished).

[12] K. Sengstock, U. Sterr, J. H. Müller, V. Rieger, D. Bettermann, and W. Ertmer, Appl. Phys. B: Lasers Opt. **59**, 99 (1994).

[13] F. Ruschewitz, J. Peng, H. Henderthur, N. Scharreath, and W. Ertmer, Phys. Rev. Lett. **80**, 3173 (1998).

[14] F. Riehle, P. Kersten, H. Schnatz, T. Trebst, G. Zinner, and J. Helmcke, Laser Phys. **8**, 664 (1998).

[15] F. Riehle, H. Schnatz, B. Lipphardt, G. Zinner, T. Trebst, and J. Helmcke, IEEE Trans. Instrum. Meas. **48**, 613 (1999).

[16] C. W. Oates, F. Bondu, R. W. Fox, and L. Hollberg, Eur. Phys. J. D **7**, 449 (1999).

[17] G. Zinner, T. Binnewies, F. Riehle, and E. Tiemann, Phys. Rev. Lett. **85**, 2292 (2000).

[18] K. Honda, Y. Takahashi, T. Kuwamoto, M. Fujimoto, K. Toyoda, K. Ishikawa, and T. Yabuzaki, Phys. Rev. A **59**, R934 (1999).

[19] T. Kuwamoto, K. Honda, Y. Takahashi, and T. Yabuzaki, Phys. Rev. A **60**, R745 (1999).

[20] M. Machholm, P. S. Julienne, and K.-A. Suominen, Phys. Rev. A **59**, R4113 (1999).

[21] P. S. Julienne, K.-A. Suominen, and Y. Band, Phys. Rev. A **49**, 3890 (1994).

[22] The positive-definite transfer function J_{ee} represents an incoming flux, including the effect of multiple vibrations, and can be greater than unity on resonance.

[23] M. J. Holland, K.-A. Suominen, and K. Burnett, Phys. Rev. Lett. **72**, 2367 (1994); Phys. Rev. A **50**, 1513 (1994).

[24] K.-A. Suominen, Y. B. Band, I. Tuvi, K. Burnett, and P. S. Julienne, Phys. Rev. A **57**, 3724 (1998).

[25] National Institute of Standards and Technology, Atomic Spec-

tra Database ([http://physics.nist.gov]).

[26] Lifetimes of ^{3}P states—Mg: A. Godone and C. Novero, Phys. Rev. A **45**, 1717 (1992); Ca: linewidth less than 300 Hz from R. Drozdowski, J. Kwela, and M. Walkiewicz, Z. Phys. D: At., Mol. Clusters **27**, 321 (1993); Sr: J. F. Kelly, M. Harris, and A. Gallagher, Phys. Rev. A **37**, 2354 (1988); Ba: J. Brust and A. Gallagher, *ibid.* **52**, 2120 (1995); Yb: Ref. [19].

[27] A. A. Radzig and B. M. Smirnov, *Reference Data on Atoms, Molecules and Ions* (Springer, Berlin, 1985).

[28] W. J. Stevens and M. Krauss, J. Chem. Phys. **67**, 1977 (1977).

[29] N. Boutassetta, A. R. Allouche, and M. Aubert-Frécon, Phys. Rev. A **53**, 3845 (1996).

[30] A. R. Allouche, M. Aubert-Frécon, G. Nicolas, and F. Spieglemann, Chem. Phys. **200**, 63 (1995).

[31] E. Czuchaj (private communication).

[32] W. J. Meath, J. Chem. Phys. **48**, 227 (1968).

[33] R. J. Leroy and R. B. Bernstein, Chem. Phys. Lett. **5**, 42 (1970); J. Chem. Phys. **52**, 3869 (1970).

[34] P. S. Julienne, J. Res. Natl. Inst. Stand. Technol. **101**, 487 (1996) [http://nvl.nist.gov].

[35] C. Boisseau, E. Audouard, J. Vigué, and P. S. Julienne, Phys. Rev. A **62**, 052705 (2000).

[36] E. E. Nikitin, in *Atomic, Molecular and Optical Physics Handbook*, edited by G. W. F. Drake (AIP Press, Woodbury, 1996), p. 567.

[37] O. Dulieu, J. Weiner, and P. S. Julienne, Phys. Rev. A **49**, 607 (1994).

[38] R. Napolitano, J. Weiner, C. J. Williams, and P. S. Julienne, Phys. Rev. Lett. **73**, 1352 (1994).

[39] P. J. Hay and J. T. H. Dunning, J. Chem. Phys. **65**, 2679 (1976).

[40] R. Napolitano, J. Weiner, and P. S. Julienne, Phys. Rev. A **55**, 1191 (1997).

[41] H. M. J. M. Boesten, B. J. Verhaar, and E. Tiesinga, Phys. Rev. A **48**, 1428 (1993); H. M. J. M. Boesten and B. J. Verhaar, *ibid.* **49**, 4240 (1994).

[42] K.-A. Suominen, M. J. Holland, K. Burnett, and P. S. Julienne, Phys. Rev. A **49**, 3897 (1994).

[43] A. Gallagher and D. E. Pritchard, Phys. Rev. Lett. **63**, 957 (1989).

[44] J. Bohn and P. S. Julienne, Phys. Rev. A **60**, 414 (1999).

[45] F. H. Mies and P. S. Julienne, J. Chem. Phys. **80**, 2526 (1984).

[46] P. S. Julienne and F. H. Mies, in *Electron and Atomic Collisions*, edited by D. C. Lorents, W. E. Meyerhof, and J. R. Petersen (North-Holland, Amsterdam, 1986).

[47] J. Tellinghuissen and P. S. Julienne, J. Chem. Phys. **81**, 5779 (1984).

[48] An error in the line strength function in our computer code resulted in magnitudes for K that were too large in Ref. [20], and the sum over l'' was truncated too soon. The qualitative results given in Ref. [20] are correct, however.

[49] R. H. Bell and M. J. Seaton, J. Phys. B **18**, 1589 (1985).

[50] Since two atoms are lost per collision, Ref. [7] reported the total atom loss rate coefficient β, which is $2K$ with our definition of K.

[51] M. Machholm, P. S. Julienne, and K.-A. Suominen, e-print physics/0107051.